Multi-objective optimization of proton exchange membrane fuel cells by RSM and NSGA-II

Zhijie Chen[a] Wei Zuo[a, d*] Kun Zhou[a, d] Qingqing Li[a, d] Yuhan Huang[b] Jiaqiang E[c]

a. The State Key Laboratory of Refractories and Metallurgy, Wuhan University of Science and Technology, Wuhan 430081, China

b. Centre for Green Technology, School of Civil and Environmental Engineering, University of Technology Sydney, NSW 2007, Australia

c. College of Mechanical and Vehicle Engineering, Hunan University, Changsha 410082, China

d. National-provincial Joint Engineering Research Center of High Temperature Materials and Lining Technology, Wuhan University of Science and Technology, Wuhan 430081, China

**zuowei@wust.edu.cn*

Graphical Abstract (for review)

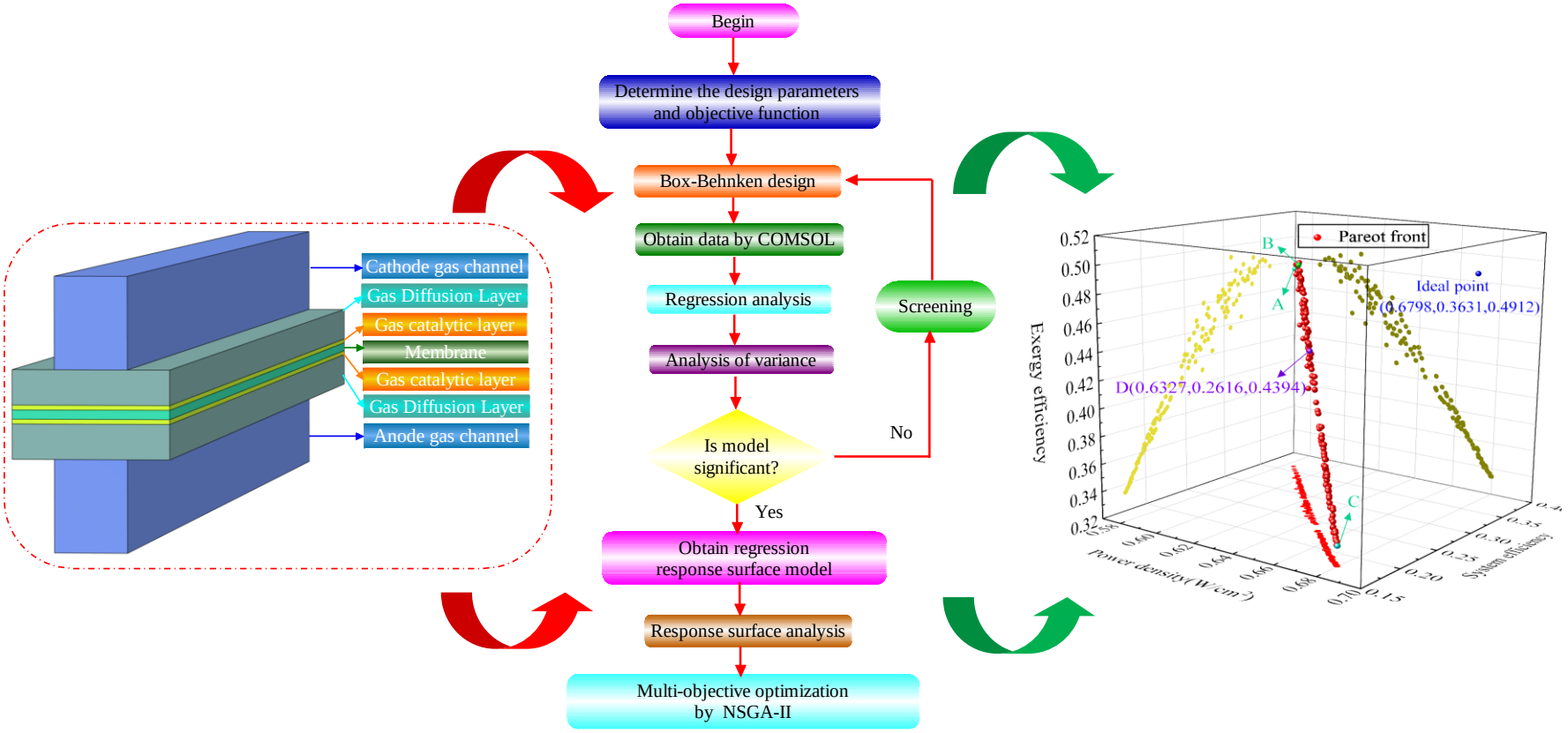

Highlights

1. The constructed regression model is verified by ANOVA.
2. RSM and NSGA-II is combined for multi-objective optimization of PEMFC.
3. Effects of interaction term on power density and system efficiency are revealed.
4. The distribution of Pareto-optimal solutions is obtained.
5. The optimal design parameters of PEMFC are determined.

Abstract: This study optimized the performance of a proton exchange membrane fuel cell by combining the response surface methodology and non-dominated ranking genetic algorithm. Firstly, the design variables are determined, including operating pressure (p), operating temperature (T), Anode stoichiometry ratio (λ_a), thickness of the proton exchange membrane (H_{mem}) and gas diffusion layer (GDL) porosity (ε_{GDL}). The objective functions are also identified, including power density (P), system efficiency (η) and exergy efficiency. Then, the Box-Behnken design is employed to arrange the numerical investigations. Analysis of variance is used to verify the appropriateness and reliability of the constructed regression models. Response surface analysis is used to show the interaction between each pair of design parameters. Finally, the Pareto optimal frontier is obtained by non-dominated ranking genetic algorithm II and the regression models constructed by response surface methodology. The Pareto optimal solution offers a power density of 0.6327 $W \cdot cm^{-2}$, a system efficiency of 26.16% and an exergy efficiency of 43.94 %, which is 13.18 %, 7.06 % and 20.29 % better than the initial direct current channel, respectively. The corresponding design variables is p=2.6498 atm, T=341.621 K, λ_a =1.1808, H_{mem} =0.0577 mm and ε_{GDL} =0.4908. This work provides a new multi-objective optimization method for designing more efficient proton exchange membrane fuel cells.

Keywords: Proton exchange membrane fuel cell; Multi-objective optimization; Response surface methodology; Non-dominated sorting genetic algorithm II

Nomenclature

A area (m^2)

C molar concentration ($mol \cdot m^{-3}$)

c_p constant pressure heat capacity ($J \cdot kg^{-1} \cdot k^{-1}$)

D mass diffusivity of species ($m^2 \cdot s^{-1}$)

ex exergy (W)

F Faraday's constant (96485C mol^{-1})

$\overline{h}$ specific enthalpy ($kJ \cdot kg^{-1}$)

H thickness

i current density ($A \cdot cm^{-2}$)

I electric current (A)

j exchange current density ($A \cdot m^{-3}$)

k thermal conductivity ($W \cdot m^{-1} \cdot k^{-1}$)

p pressure (atm)

p_{in} inlet air pressure to the compressor

P power density($W \cdot cm^{-2}$)

r condensing rate ($kg \cdot m^{-2} \cdot s^{-1}$)

R universal gas constant (8.314 $J \cdot mol^{-1} \cdot K^{-1}$)

R^2 coefficient of determination

$\overline{s}$ specific entropy ($kJ \cdot mol^{-1} \cdot K^{-1}$)

T_e entry air temperature (K)

T temperature (K)

33

W power (W)

$\vec{u}$ velocity ($m \cdot s^{-1}$)

x Mass fraction

Greek letters

α transfer coefficient

β overpotential (V)

ε porosity

μ viscosity ($Pa \cdot s^{-1}$)

ρ density ($kg \cdot m^{-3}$)

η efficiency

η_c compressor connecting efficiency

η_{mt} motor efficiency

σ conductivity ($S \cdot m^{-1}$)

φ phase potential (V)

λ stoichiometric ratio

γ specific heat ratio

$\square$ exergy efficiency

subscripts

a anode

c cathode

ch chemical exergy

eff effective

H_2 Hydrogen

34

in	inlet
l	liquid phase
i	species (H_2, O_2, H_2O)
w	water
mem	membrane
O_2	oxygen
ref	reference
s	solid phase

Abbreviations

ANOVA	Analysis of variance
BPP	bipolar plate
CFD	computational fluid dynamics
CL	catalytic layer
GDL	gas diffusion layer
LHV	lower heating value of hydrogen (2.4×10^5 J·mol^{-1})
NSGA-II	non-dominated sorting genetic algorithm 2
PEMFC	proton exchange membrane fuel cell
RSM	response surface methodology
RH	relative humidity
UAV	unmanned aerial vehicle

1. Introduction

Nowadays, fuel cells are considered a renewable energy source and have been used as power sources for many mechanical devices because they are environmentally friendly, reliable and efficient [1-3]. Among various types of fuel cells, proton exchange membrane fuel cells (PEMFCs) perform better in terms of specific energy density, conversion efficiency, transient response and operating temperatures [4-7]. However, there are still many key challenges for PEMFCs before large-scale commercialization, such as reducing cost [8-10], improving durability [11-13], and increasing power density [14-16].

Investigations were carried out on performance optimization of PEMFC to address the above issues [17-21]. Seyhan et al. [22] showed that the maximum power of a serpentine flow channel with the lowest amplitude was increased by 20.15 % compared to the conventional serpentine flow channel at 0.7 SLPM H_2 and 1.5 SLPM air. Saleh et al. [23] investigated the operation of a PEMFC unmanned aerial vehicle (UAV) in a high-altitude environment. Ubong et al. [24] simulated the performance of a single cell with three serpentine flow channels at different temperatures, pressures, and air stoichiometry ratios. The results showed that the theoretical model could accurately predict the experimental results. Haraldsson et al. [25] explored the effect of environmental causal conditions on the performance of fuel cell vehicles. Ghasabehi et al. [26] studied the porosity of different working pressures, temperatures, stoichiometry and gas diffusion layers (GDL). They found that porosity and pressure played an important role in determining the water saturation focal and resistance. Li et al. [27] proposed that the thickness of the proton exchange membrane had an important effect on power density, efficiency and oxygen homogeneity at different proton exchange membranes. Son et al. [28] investigated the effect of anisotropic GDL porosity on PEMFCs with different flow channels. Cho et al. [29] investigated the effect of temperature, relative humidity and cathode stoichiometry on the dynamic response of voltage at different current variations. Sim et al. [30] systematically investigated

the effects of operating temperature, hydrogen humidification, cathode opening zone orientation, and GDL substrate thickness on OC-PEMFC performance.

Furthermore, system and exergy efficiencies of PEMFCs were extensively investigated [31-33]. Authayanun et al. [34] analyzed the effects of temperature, pressure and stoichiometry ratios of anode and cathode on battery efficiency and performance. Chen et al. [35] studied the effect of auxiliary equipment energy consumption on fuel cell power system efficiency and total system cost under dynamic operating conditions. Midilli et al. [36] investigated the effect of irreversibility on the thermodynamic properties of PEMFC under different operating conditions. The results showed that increasing the thickness of the membrane would reduce the exergy efficiency of the PEMFC. Kazim et al. [37] performed an integrated exergy analysis under variable operating temperature, pressure, cell voltage and air stoichiometry. Luo et al. [38] comprehensively analyzed the energy consumption, emissions and economics of methanol, electric, gas and gasoline vehicles. Zhao et al. [39] investigated the effect of PEMFC operating parameters and refrigeration system on the energy, exergy, economy and environment (4Es).

Multi-objective optimization is critical for obtaining a better comprehensive performance of PEMFCs. Kanani et al. [40] used the central composite second-order response surface method (RSM) to model the effects of various parameters on the power. The results showed that optimal performance could be achieved under certain values of cathode stoichiometry, anode stoichiometry and relative humidity. Li et al. [41] proposed a fast and systematic optimization method by combining ANOVA, substitution model and non-dominated ranking genetic algorithm (NSGA-II) to reduce common PEMFC parameters from eleven to six. An optimization procedure combining NSGA-II and substitution model was also introduced, which took only 9 min 37 s to complete the multi-objective optimization. Silva et al. [42] combined RSM with error propagation to provide an efficient robust

design, which could find the best working conditions, maximize the power density and reduce the normal working variability of PEMFC. Sohani et al. [43] proposed an objective function based on one possible combination of efficiency, power density, levelized cost and size. The best solution based on four preference criteria for traffic and stationary applications was selected by comparing the optimal answers of different scenarios. The effect of capacity variation on decision and the corresponding values of the four performance criteria were also investigated. Yao et al. [44] investigated multiple objectives for the performance optimization of a PEMFC by verifying the feasibility of water recovery and the effect of pressure, temperature and relative humidity on the electrochemical performance and water recovery performance. Chen et al. [45] applied a new evolutionary algorithm (MOEA/D) for system optimization and discussed the system performance under different operating conditions.

As reviewed above, multi-objective optimization is an effective tool to help improve the comprehensive performance of PEMFCs. However, it is necessary to understand the interaction effects of different factors on the performance of PEMFCs for the multi-objective optimization. To fill this knowledge gap, this work combined the RSM and NSGA-II to obtain the optimal power density, system efficiency and external energy efficiency of PEMFCs. This work provides a new method for multi-objective optimization of PEMFCs.

2. PEMFC Model

2.1. Physical model

In this work, a three-dimensional geometry of a single-channel PEMFC is constructed by SOLIDWORKS (Figure 1). The geometric parameters are presented in Table 1. The model includes seven components, i.e. cathode gas channel, anode gas channel, gas catalytic layer, GDL, and proton

exchange membrane [46]. In the anode catalytic layer, hydrogen is catalytically decomposed into protons, which reach the cathode through the proton exchange membrane. The electrons generated by hydrogen decomposition go to the cathode through the load, which can generate electricity.

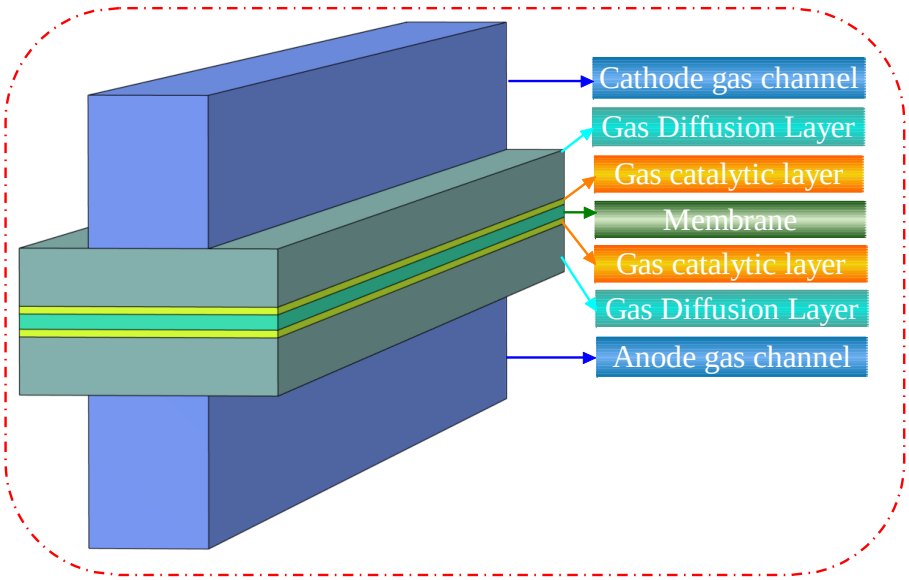

Figure 1 Geometry of a single-channel PEMFC.

Table 1 Geometric parameters

Parameters	Value (mm)	Ref
Channel width	0.7874	[24]
Channel depth	1.0	[24]
Channel length	20.0	[24]
Rib width	0.90932	[24]
Cell width	2.0	[24]
GDL thickness	0.38	[24]
CL thickness	0.05	[24]
Membrane thickness	0.1	[24]

2.2. Governing equations

Assumptions are made to simplify the mathematical model of PEMFC [40]. Firstly, the PEMFC works under steady state. Secondly, the flow in the gas channel is incompressible stratified flow with constant physical parameters. Thirdly, the gas mixture is considered ideal gas. Finally, the membrane, CL and GDL are isotropic porous mediums. Thus, the governing equations of continuity, momentum, energy, species and charge conservation are as follows:

Continuity equation [40]:

$$\nabla \cdot (\rho \vec{u}) = 0 \quad (1)$$

Momentum equation [40]:

$$\frac{1}{\varepsilon^2} \nabla \cdot (\rho \vec{u} \vec{u}) = -\nabla p + \frac{1}{\varepsilon} \nabla \cdot (\mu \nabla \vec{u}) + S_{\mathrm{u}} \quad (2)$$

where p is the pressure, μ is the viscosity, and S_{u} is the momentum source term, for GDL and CL,

$$S_{\mathrm{u}} = -\frac{\mu}{K} \varepsilon^2 \vec{u} \quad (3)$$

Energy equation [52]:

$$\varepsilon \rho c_{\mathrm{p}} \vec{u} \cdot \nabla T = \nabla \cdot (k_{\mathrm{eff}} \nabla T) + S_{\mathrm{h}} \quad (4)$$

where c_{p} is the constant pressure specific heat, T is the temperature, k_{eff} is the effective thermal conductivity, and S_{h} is the energy term.

$$k_{\mathrm{eff}} = \varepsilon k_{\mathrm{l}} + (1 - \varepsilon) k_{\mathrm{s}} \quad (5)$$

$$S_{\mathrm{h}} = h_{\mathrm{react}} + j_{\mathrm{a,c}} \eta_{\mathrm{a,c}} + I^2 R_{\mathrm{ohm}} + r_{\mathrm{w}} h_{\mathrm{l}} \quad (6)$$

where k_{l} is the thermal conductivity of the fluid and k_{s} is the thermal conductivity of the solid.

Species conservation equation [40]:

$$\nabla \cdot (\varepsilon \vec{u} C_{\mathrm{i}}) = \nabla \cdot \left(D_{\mathrm{i,eff}} \nabla C_{\mathrm{i}} \right) + S_{\mathrm{i}} \quad (7)$$

where C_{i} is the volume fraction of different species, S_{i} is the species source term, and $D_{\mathrm{i,eff}}$ is the effective diffusivity of the species which represents the effect of porous media and can be expressed as follows:

$$D_{\mathrm{i,eff}} = \varepsilon^{1.5} (1 - s)^{2.5} D_{\mathrm{i}}^{0} \left(\frac{101325}{p} \right) \left(\frac{T}{300} \right)^{1.5} \quad (8)$$

Charge conservation equation [40]:

$$\nabla \cdot \left(\sigma_{\mathrm{s}} \nabla \varphi_{\mathrm{s}} \right) + S_{\mathrm{s}} = 0 \quad (9)$$

$$\nabla \cdot (\sigma_{\mathrm{m}} \nabla \varphi_{\mathrm{m}}) + S_{\mathrm{m}} = 0 \quad (10)$$

where σ_s and σ_m are the conductivity of the solid region and the membrane, respectively, φ_s and φ_m are the phase potentials of the solid region and the membrane, respectively, and S_s and S_m are the volume transfer currents of the solid region and the membrane, respectively. σ_m can be described as:

$$\sigma_m = (0.514\omega - 0.326)e^{1268\left(\frac{1}{303}-\frac{1}{T}\right)} \quad (11)$$

where ω is the water content of the membrane and T is the temperature.

Sources terms in the electron and proton transport equations are derived from electrochemical reactions that occur only at the anode and cathode catalyst layers and are presented as:

Anodic catalytic layer:

$$S_m = j_a \quad S_s = -j_a \quad (12)$$

Cathodic catalytic layer:

$$S_m = j_c \quad S_s = -j_c \quad (13)$$

where j_a and j_c are the transfer current densities corresponding to the electrochemical reactions at the anode and cathode catalyst layers, respectively.

The source terms in both the substance and charge equations are related to the transfer current densities j_a and j_c, which are calculated by the simplified Butler-Volmer equation:

$$j_a = ai_{0,a}^{ref}\left(\frac{C_{H_2}}{C_{H_2,ref}}\right)^{0.5}\left(\frac{\alpha_a + \alpha_c}{RT}F\beta_a\right) \quad (14)$$

$$j_c = ai_{0,c}^{ref}\left(\frac{C_{O_2}}{C_{O_2,ref}}\right)exp\left(-\frac{\alpha_c}{RT}F\beta_c\right) \quad (15)$$

where β denotes the potential difference between the solid substrate and the electrolyte, defined as:

Anode side:

$$\beta_a = \varphi_s - \varphi_m \quad (16)$$

Cathode side:

$$\beta_c = \varphi_s - \varphi_m - U_{oc} \quad (17)$$

where U_{oc} is the open circuit potential.

2.3. Numerical scheme

COMSOL Multiphysics is used to solve the above governing equations. The inlet velocities of anode and cathode flow channels are kept constant. The inlet gas velocities are calculated based on stoichiometric ratios, fuel cell active area and flow channel dimensions [24]:

$$\vec{u}_{\text{in\_c}} = \frac{\lambda_{\text{c}} \frac{I}{4F} x_{\text{o}_2} RT}{p \cdot A_{\text{channel}}} \tag{18}$$

$$\vec{u}_{\text{in\_a}} = \frac{\lambda_{\text{a}} \frac{I}{4F} x_{\text{H}_2} RT}{p \cdot A_{\text{channel}}} \tag{19}$$

The reference pressure is set to atmospheric pressure at the outlet of the flow channel. Symmetric boundary conditions are applied at the left and right sides of the GDL and CL. No-slip boundary condition is employed at the other walls [24]. The voltage of the anode receiver is set to zero and the cathode receiver is set to 0.95 V. During the simulations, the cathode voltage value is varied between 0.95 and 0.4 V with an interval of 0.05 V [41].

2.4. Grid independence study

The effect of grid number on voltage and current density was examined to obtain a proper grid size for the optimal computational cost and calculation accuracy. As shown in Figure 2, the current density difference between 5056 and 19708 grids at 0.2 V is 10.08 %. However, the three polarization curves of 19708, 78648 and 124644 grids almost overlap. Therefore, the calculation results are independent of the grids when the grid number is larger than 19708. Considering the calculation time and accuracy, the model with the grid number of 19708 is chosen in this work.

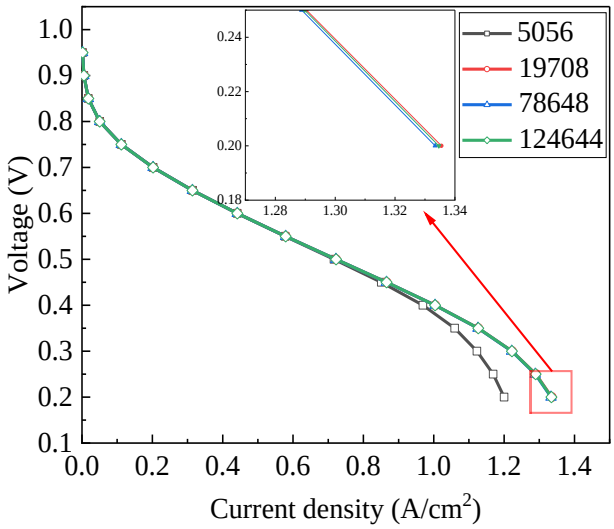

Figure 2 Effect of grid size on voltage and current density.

2.5. Model validation

To verify the model, the simulation results are compared with the experimental data [24] under the same working conditions. The geometric parameters of the model are the same as those of the experimental device (Table 2). The experimental and numerical results under different pressure conditions are shown in Figure 3. The CFD results agree well the experimental data. The error is within an acceptable range, indicating that the model is feasible in this work.

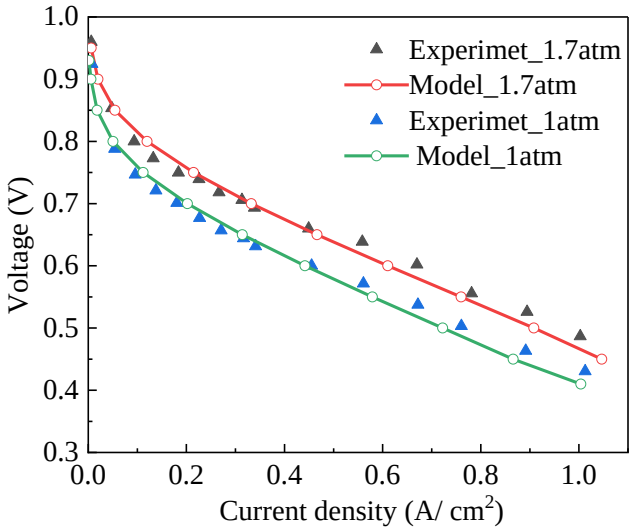

Figure 3 Model validation.

Table 2 Main operating parameters of the PEMFC

Parameter	Value	Ref

Entry air temperature (T_e) (K)	301.15	[24]
Fuel cell temperature (T) (K)	453.15	[24]
Reference ambient temperature(T_0)(K)	293.15	[49]
Anode inlet gas flow rate (λ_a)	1.2	[24]
Cathode inlet gas flow rate (λ_c)	2	[24]
Backpressure (Pa)	101325	[24]
Membrane conductivity ($S \cdot m^{-1}$)	9.825	[24]
Membrane permeability (m^2)	1.80E-11	[24]
Gas diffusion layer conductivity ($S \cdot m^{-1}$)	222	[24]
Gas diffusion layer permeability (m^2)	2.36E-12	[24]
Mass fraction of H_2O at cathode	0.037319	[24]
Mass fraction of O_2 at cathode	0.20216	[24]
Mass fraction of H_2 at anode	0.96268	[24]
Open-circuit voltage (V)	0.95	[24]
Anode exchange current density ($A \cdot m^{-2}$)	1.00E+02	[24]
Cathode exchange current density ($A \cdot m^{-2}$)	1.00E-03	[24]
GDL porosity	0.4	[24]
CL surface-to-volume ratio (1/m)	1.00E+07	[24]
Cathode transfer coefficient	1	[24]
Compressor efficiency (η_c)	0.85	[45]
Inlet pressure (p_{in}) (atm)	1	[45]
Motor efficiency (η_{mt})	0.85	[45]
Specific heat constant of air (c_p) ($J \cdot K^{-1} \cdot kg^{-1}$)	1004	[45]
Standard chemical exergy of hydrogen ($\boldsymbol{ex}^{\mathbf{ch}}_{\mathbf{H_2}}$)($kJ \cdot kmol^{-1}$)	235150	[50]
Standard chemical exergy of oxygen ($\boldsymbol{ex}^{\mathbf{ch}}_{\mathbf{O_2}}$)($kJ \cdot kmol^{-1}$)	3970	[49]
Standard chemical exergy of nitrogen ($\boldsymbol{ex}^{\mathbf{ch}}_{\mathbf{N_2}}$)($kJ \cdot kmol^{-1}$)	720	[49]
Standard chemical exergy of water ($\boldsymbol{ex}^{\mathbf{ch}}_{\mathbf{H_2O}}$)($kJ \cdot kmol^{-1}$)	3120	[49]

3. Multi-objective optimization

3.1. Response surface methodology

The RSM developed by Box and Wilson in 1951 [48] is a statistical method to solve multivariate

problems by using a reasonable experimental design method and obtaining certain data through experiments. It employs a multiple quadratic regression equation to fit the functional relationship between factors and response values. The optimal process parameters are identified through the analysis of the regression equation. The relationship between the objective function G and the design variables x_1, x_2, ..., x_k is expressed as:

$$G = f(x_1, x_2, \ldots x_k) + \varepsilon \quad (20)$$

where f denotes the approximation function and ε denotes the residual error between the actual value and the approximation value. The approximation function can be a quadratic polynomial function reflecting the nonlinear relationship between the target function and the design variables. The quadratic polynomial function containing the linear, squared and interaction terms is expressed as:

$$G = a_0 + \sum_{i=1}^{k} a_i x_i + \sum_{i=1}^{k} a_{ii} x_i^2 + \sum_{i \le j} a_{ij} x_i x_j + \varepsilon \quad (21)$$

where a_0, a_i, a_{ii}, and a_{ij} denote the intercept regression coefficient, the linear effect of x_i, the quadratic effect of x_i, and the linear interaction effect between x_i and x_j, respectively.

3.1.1. Design variables

Previous studies [22] found that the operating temperature (T), operating pressure (p), Anode stoichiometry ratio (λ_a), porosity of the GDL (ε_{GDL}), and thickness of the membrane (H_{mem}) were the main factors affecting the performance of the PEMFC. Therefore, this study selected these five design variables for optimization. As shown in Table 3, each design variable has three levels which were chosen based on the general range of PEMFC parameters and some experience [51].

Table 3 The design variables and levels

Factor	Level A	Level B	Level C
Operating pressure (P) (atm)	1	2	3
Operating temperature (T) (K)	333	343	353
Anode stoichiometry ratio (λ_a)	1	1.5	2

Membrane thickness (H_{mem}) (mm)	0.05	0.1	0.15
GDL porosity (ε_{GDL})	0.3	0.4	0.5

3.1.2. Objective functions

The objective function in this work includes the power density (W·cm^{-2}), system efficiency (%) and exergy efficiency (%).

The power density is defined as [52]:

$$w = iV \tag{22}$$

where i is the current density of the PEMFC and V is the corresponding voltage.

The system efficiency is:

$$\eta = \frac{W - W_{\mathrm{prs}}}{W_{\mathrm{fuel}}} \tag{23}$$

where W is the output power of PEMFC, W_{prs} stands for parasitic power and W_{fuel} is the inherent power of the fuel. They are expressed as:

$$W = wA \tag{24}$$

$$W_{\mathrm{prs}} = W_{\mathrm{comp}} + W_{\mathrm{others}} \tag{25}$$

$$W_{\mathrm{fuel}} = \lambda_{\mathrm{a}} \frac{iA}{2F} LHV \tag{26}$$

where λ_{a} is the stoichiometric ratio of the anode, W_{comp} is the power consumption of the compressor, and W_{others} are other power losses:

$$W_{\mathrm{comp}} = \frac{c_{\mathrm{p}} T_{\mathrm{e}}}{\eta_c \eta_{\mathrm{mt}}} \left[\left(\frac{p}{p_{\mathrm{in}}}\right)^{0.286} - 1\right] m_{\mathrm{air}} \tag{27}$$

$$m_{\mathrm{air}} = 3.57 \times 10^{-7} \lambda_{\mathrm{c}} iA \tag{28}$$

$$W_{\mathrm{others}} = 0.05W \tag{29}$$

Some parameters in the above equations are assumed to be constant although they may vary with compressor size and full load ratio. However, this does not affect the optimization procedure, and similar assumption was made in the previous studies [42,52].

The system has the ability to do work externally when there is an imbalance between the

chemical potential, concentration, and electromagnetic field of the given position between the thermodynamic system and the environment. Exergy is the part of energy that can theoretically be infinitely converted to any other form of energy when the system is reversibly changed from an arbitrary state to a state in equilibrium with the given environment. Any irreversible process is subject to exergy loss. Therefore, in mathematics, the exergy balance can be calculated by the following equation [49, 50, 53, 54]:

$$\sum \dot{E} x_{\mathrm{in}}^{\mathrm{fc}} = \sum \dot{E} x_{\mathrm{fav,out}}^{\mathrm{fc}} + \sum \dot{E} x_{\mathrm{RWE}}^{\mathrm{fc}} + \sum \dot{E} x_{\mathrm{UWE}}^{\mathrm{fc}} + \sum \dot{E} x_{\mathrm{des}}^{\mathrm{fc}} \tag{30}$$

where $\sum \dot{E}\, x_{\mathrm{fav,out}}^{\mathrm{fc}}$, $\sum \dot{E}\, x_{\mathrm{RWE}}^{\mathrm{fc}}$, $\sum \dot{E}\, x_{\mathrm{UWE}}^{\mathrm{fc}}$ and $\sum \dot{E}\, x_{\mathrm{des}}^{\mathrm{fc}}$ represent favorable exergy, reusable waste exergy, unavailable waste exergy, and destructive exergy, respectively.

Exergy can be decomposed into various components. In PEMFCs, kinetic and potential exergy can be neglected. So the total exergy can be written as:

$$ex_{\mathrm{i}} = ex_{\mathrm{tm}} + ex_{\mathrm{ch}} \tag{31}$$

The thermal potential energy is defined as:

$$ex_{\mathrm{tm}} = (\overline{h} - \overline{h_0}) - T_0\,(\overline{s} - \overline{s_0}) \tag{32}$$

where h and s denote the specific enthalpy and the entropy, respectively. The reference ambient temperature and pressure are 298 K and 1 atm, respectively. The thermal potential exergy of an ideal gas with constant specific heat capacity and constant specific heat ratio is expressed as:

$$ex_{\mathrm{tm}} = c_{\mathrm{p}} T_0 \left[\frac{T}{T_0} - 1 - \ln\left(\frac{T}{T_0}\right) + \ln\left(\frac{p}{p_0}\right)^{\frac{\gamma-1}{\gamma}}\right] \tag{33}$$

where the specific heat capacity and the specific heat ratio are given in Table 4 [49, 50].

Chemical potential exergy is the result of a compositional imbalance between the substance and the other parameters of the medium. It is defined as:

$$ex_{\mathrm{ch}} = x_{\mathrm{i}}(ex_{\mathrm{i}})^{\mathrm{ch}} + RT_0 x_{\mathrm{i}} \ln(x_{\mathrm{i}}) \tag{34}$$

where x_{i} and $(ex_{\mathrm{i}})^{\mathrm{ch}}$ represent the molar fraction and the chemical potential energy of species i in

the standard state, respectively. The favorable exergy is defined as:

$$\sum \dot{E}\, x_{\mathrm{fav,out}}^{\mathrm{fc}} = W \tag{35}$$

The exergy efficiency equation is:

$$\psi_{\mathrm{ex}} = \frac{W}{(\dot{n} \times ex)_{\mathrm{H2,in}} + (\dot{n} \times ex)_{\mathrm{O2,in}}} \tag{36}$$

Table 4 Specific heat capacity and specific heat ratio

Material	c_p (kJ·kg^{-3}·K^{-1})	ρ (kg·m^{-3})	$\boldsymbol{\gamma}$
Hydrogen	13602.45+3.402317·T -0.003358423·T^2 -3.907953·10^{-7}·T^3 +1.705345·10^{-9}·T^4	1.46	1.409
Oxygen	834.8265+0.292958·T -0.0001495637·T^2+3.41389·10^{-7}·T^3 -2.278359·10^{-10}·T^4	1.299	1.393
Nitrogen	979.043+0.4179639·T - 0.001176279·T^2+1.674394*10^{-6}·T^3 -7.256297·10^{-10}·T^4	1.138	1.400
Water vapor	1563.077 + 1.603755·T -0.002932784·T^2 + 3.216101·10^{-6}·T^3 −1.156827 ·10^{-6}·T^4	0.5542	1.327
Liquid water	4182	988.2	—

3.1.3. Optimization process

Figure 4 shows the flow diagram of the optimization procedure used in this work. Box-Behnken design (BBD) is an experimental design method that can evaluate the nonlinear relationship between indicators and factors. Unlike the central composite design, it does not require multiple consecutive trials and is more economical than the central composite design because the number of test combinations in a Box-Behnken test is less than that in a traditional composite design when the number of factors is the same. The corresponding results for the Box-Behnken design are listed in Table 4. Analysis of variance (ANOVA) is used to verify the appropriateness and reliability of the constructed regression models. Response surface analysis is conducted to show the interaction between each pair of design parameters. A regression model constructed by RSM is performed for multi-objective optimization utilizing the non-dominated ranking genetic algorithm II (NSGA-II).

The optimal design parameters are determined using the Pareto optimal solution.

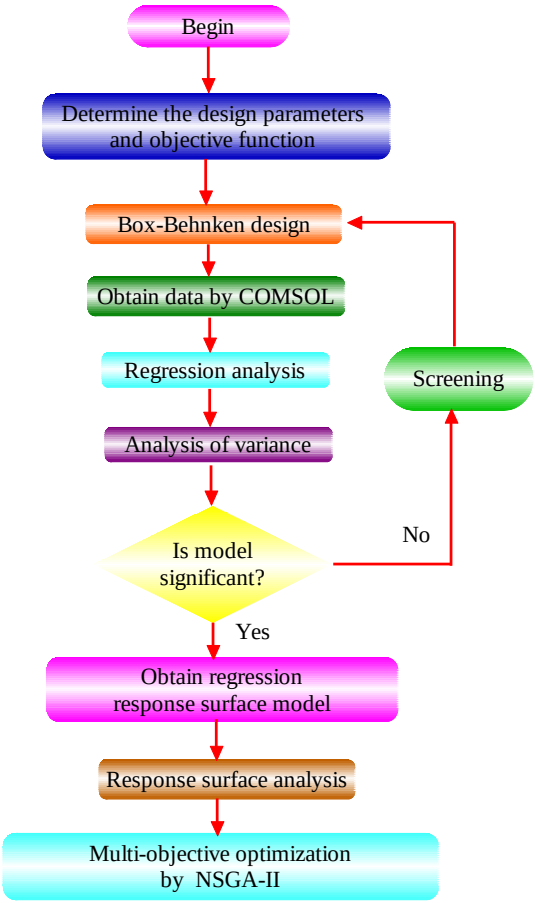

Figure 4 Flow chart of optimization procedure.

279

Table 4 Results of Box-Behnken design

Case number	Operating pressure (atm)	Operating temperature (K)	Anode stoichiometry ratio	Membrane thickness (mm)	GDL porosity	Power density ($W \cdot cm^{-2}$)	System efficiency	Exergy efficiency
1	2	333	1.5	0.1	0.3	0.5175	0.2195	0.3207
2	2	343	1.5	0.1	0.4	0.5871	0.2195	0.3298
3	2	333	2	0.1	0.4	0.5915	0.1646	0.3073
4	2	353	1.5	0.1	0.5	0.60995	0.2195	0.3246
5	2	343	1.5	0.1	0.4	0.5871	0.2195	0.4667
6	1	343	1.5	0.15	0.4	0.52415	0.2546	0.2575
7	2	333	1.5	0.05	0.4	0.6223	0.2195	0.44
8	2	343	1.5	0.15	0.3	0.50105	0.2195	0.2306
9	2	353	1.5	0.05	0.4	0.6227	0.2195	0.2849
10	2	343	2	0.15	0.4	0.5584	0.1646	0.2831
11	3	343	1.5	0.15	0.4	0.57335	0.1955	0.3451
12	2	353	1	0.1	0.4	0.54775	0.3293	0.335
13	2	353	2	0.1	0.4	0.5813	0.1646	0.4539
14	2	343	1.5	0.05	0.3	0.53455	0.2195	0.4579
15	2	343	1.5	0.1	0.4	0.5871	0.2195	0.2365
16	2	343	1.5	0.1	0.4	0.5871	0.2195	0.2457
17	2	343	1	0.1	0.3	0.5132	0.3293	0.294
18	2	343	1.5	0.05	0.5	0.66745	0.2195	0.2755
19	2	353	1.5	0.1	0.3	0.51545	0.2195	0.367
20	2	343	1	0.1	0.5	0.56205	0.3293	0.32
21	1	343	1.5	0.1	0.5	0.5822	0.2546	0.4573
22	2	343	1.5	0.1	0.4	0.5871	0.2195	0.4498
23	1	343	2	0.1	0.4	0.55895	0.191	0.2446
24	1	343	1.5	0.1	0.3	0.50125	0.2546	0.2398
25	2	343	1.5	0.1	0.4	0.5871	0.2195	0.3418

26	2	343	2	0.1	0.3	0.51625	0.1646	0.3431
27	3	343	1.5	0.05	0.4	0.62975	0.1955	0.2954
28	3	333	1.5	0.1	0.4	0.60465	0.1955	0.3124
29	1	333	1.5	0.1	0.4	0.56835	0.2546	0.4221
30	3	343	1.5	0.1	0.5	0.64005	0.1955	0.2132
31	2	353	1.5	0.15	0.4	0.54845	0.2195	0.4623
32	3	343	1	0.1	0.4	0.5623	0.2933	0.2561
33	1	353	1.5	0.1	0.4	0.5461	0.2546	0.2825
34	3	343	2	0.1	0.4	0.60025	0.1466	0.286
35	2	343	2	0.1	0.5	0.62005	0.1646	0.3281
36	2	343	1.5	0.15	0.5	0.5819	0.2195	0.3487
37	2	343	1	0.15	0.4	0.53495	0.3293	0.3427
38	2	333	1	0.1	0.4	0.5552	0.3293	0.342
39	1	343	1	0.1	0.4	0.5381	0.3819	0.3116
40	3	353	1.5	0.1	0.4	0.59665	0.1955	0.3012
41	2	333	1.5	0.1	0.5	0.6267	0.2195	0.3229
42	2	343	2	0.05	0.4	0.6235	0.1646	0.3229
43	1	343	1.5	0.05	0.4	0.60655	0.2546	0.3229
44	2	343	1	0.05	0.4	0.56745	0.3293	0.3229
45	3	343	1.5	0.1	0.3	0.525	0.1955	0.3229
46	2	333	1.5	0.15	0.4	0.56585	0.2195	0.3229

280

3.2. NSGA-II algorithm

NSGA-II algorithm was proposed by Srinivas and Deb in 2000 on the basis of NSGA. It adopts a fast non-dominated sorting algorithm. The computational complexity is greatly reduced than NSGA. It adopts crowding degree and crowding degree comparison operator instead of shared radius which needs to be specified. The peer comparison after fast sorting is the winning criterion, so that the individuals in the quasi-Pareto domain can be extended to the whole Pareto domain and uniformly distributed to maintain the diversity of the population. The elite strategy is introduced to expand the sampling space, preventing the loss of the best individuals and improving the computational speed and robustness of the algorithm.

Figure 5 shows the flow chart of NSGA-II. Firstly, RSM is used to obtain the objective function. Secondly, crossover and variance genetic operators are applied to generate new populations. Thirdly, an elite strategy is used in each cycle to rescue the majority of the new population. Finally, the optimization process is wrapped with a repetition count condition. The algorithm uses two functions, namely the non-dominated sorting function and the crowding distance function. In particular, the non-dominated sorting is a cyclic hierarchical process.

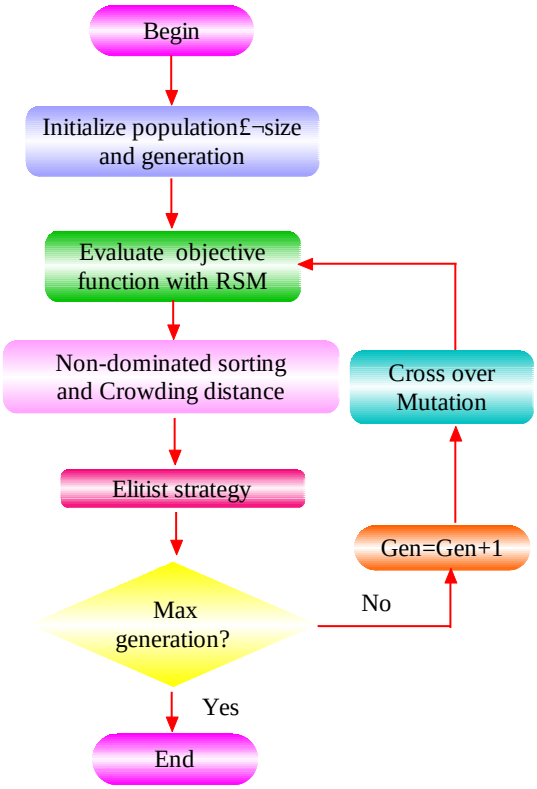

Figure 5 Flowchart of NSGA-II

4. Results and discussion

4.1. Analysis of variance

ANOVA is applied to assess the fitness of the regression model and perform significance tests. The fit of the regression model was estimated from the value of R^2 which was calculated as the sum of squares of the regression model divided by the total sum of squares. R^2(appropriate), R^2(predicted), and R^2(adjusted) indicate the superiority of fit, the superiority of fit according to the prediction of the return equation model, and the superiority of fit after adjusting for precision, respectively. The significance of each term in the regression model is indicated by the F and P values. F is calculated as the ratio between the mean square of the factor and the mean square of the error, while P is the probability value of the F test. Usually, P and F of the most significant model are the minimum and maximum values, respectively.

As shown in Table 5, the F-value of the regression model for *P* is 41.54, and the P-value of the regression model for *P* is less than 0.0001. This indicates that the model fits well and can be used to

predict P. In Table 6, the F-value of the regression model for η is 33.14, and the P-value of the regression model for η is less than 0.0001. So the model can also be used to predict η. Similarly, in Table 7, the regression F-value for exergy is 770.24 with a P-value less than 0.0001, which also indicates a high correlation between the observed and predicted values.

Table 5 Analysis of variable for P

Source	Sum of Squares	Degrees of freedom	Mean Square	F-value	P-value	
Model	0.0701	20	0.0035	89.82	< 0.0001	significant
T	0.0059	1	0.0059	150.22	< 0.0001	
p	0.0004	1	0.0004	11.21	0.0026	
λ_a	0.0045	1	0.0045	115.99	< 0.0001	
H_{mem}	0.0148	1	0.0148	378.29	< 0.0001	
ε_{GDL}	0.0367	1	0.0367	939.40	< 0.0001	
$T \cdot p$	0.0001	1	0.0001	1.30	0.2650	
$T \cdot \lambda_a$	0.0001	1	0.0001	1.87	0.1834	
$T \cdot H_{mem}$	0.0002	1	0.0002	4.33	0.0479	
$T \cdot \varepsilon_{GDL}$	0.0003	1	0.0003	7.44	0.0115	
$p \cdot \lambda_a$	1.891E-06	1	1.891E-06	0.0484	0.8276	
$p \cdot H_{mem}$	0.0001	1	0.0001	2.03	0.1667	
$p \cdot \varepsilon_{GDL}$	0.0001	1	0.0001	1.38	0.2506	
$\lambda_a \cdot H_{mem}$	0.0003	1	0.0003	6.80	0.0151	
$\lambda_a \cdot \varepsilon_{GDL}$	0.0008	1	0.0008	19.33	0.0002	
$H_{mem} \cdot \varepsilon_{GDL}$	0.0007	1	0.0007	17.35	0.0003	
T^2	0.0003	1	0.0003	8.90	0.0063	
p^2	0.0000	1	0.0000	0.2613	0.6137	
λ_a^2	0.0025	1	0.0025	63.44	< 0.0001	
H_{mem}^2	0.0001	1	0.0001	1.30	0.2645	
ε_{GDL}^2	0.0029	1	0.0029	74.29	< 0.0001	
Residual	0.0010	25	0.0000			
Lack of Fit	0.0010	20	0.0000			
Pure Error	0.0000	5	0.0000			
Cor Total	0.0711	45				
Standard deviation=0.0062						
Predicted residual error of sum of squares (PRESS)=38.2532						
R^2 (Adequate)=98.63% R^2(Predicted)=97.53% R^2(Adjusted)=94.51%						

Table 6 Analysis of variable for η

Source	Sum of Squares	Degrees of freedom	Mean Square	F-value	P-value	
Model	0.1330	20	0.0067	3042.48	< 0.0001	significant
T	0.0149	1	0.0149	6796.69	< 0.0001	
p	0.0000	1	0.0000	0.0000	1.0000	
λ_a	0.1099	1	0.1099	50248.87	< 0.0001	
H_{mem}	0.0000	1	0.0000	0.0000	1.0000	
ε_{GDL}	0.0000	1	0.0000	0.0000	1.0000	
$T \cdot p$	0.0000	1	0.0000	0.0000	1.0000	
$T \cdot \lambda_a$	0.0005	1	0.0005	223.40	< 0.0001	
$T \cdot H_{mem}$	0.0000	1	0.0000	0.0000	1.0000	
$T \cdot \varepsilon_{GDL}$	0.0000	1	0.0000	0.0000	1.0000	
$p \cdot \lambda_a$	0.0000	1	0.0000	0.0000	1.0000	
$p \cdot H_{mem}$	0.0000	1	0.0000	0.0000	1.0000	
$p \cdot \varepsilon_{GDL}$	0.0000	1	0.0000	0.0000	1.0000	
$\lambda_a \cdot H_{mem}$	0.0000	1	0.0000	0.0000	1.0000	
$\lambda_a \cdot \varepsilon_{GDL}$	0.0000	1	0.0000	0.0000	1.0000	
$H_{mem} \cdot \varepsilon_{GDL}$	0.0000	1	0.0000	0.0000	1.0000	
T^2	0.0003	1	0.0003	130.83	< 0.0001	
p^2	2.970E-08	1	2.970E-08	0.0136	0.9082	
λ_a^2	0.0067	1	0.0067	3046.30	< 0.0001	
H_{mem}^2	2.970E-08	1	2.970E-08	0.0136	0.9082	
ε_{GDL}^2	2.970E-08	1	2.970E-08	0.0136	0.9082	
Residual	0.0001	25	2.186E-06			
Lack of Fit	0.0001	20	2.733E-06			
Pure Error	0.0000	5	0.0000			
Cor Total	0.1331	45				
Standard deviation=0.0017						
Predicted residual error of sum of squares (PRESS)=202.5073						
R^2(Adequate) = 99.96 % R^2(Predicted) = 99.84 % R^2(Adjusted) = 99.93 %						

318

319 Table 7 Analysis of variable for ψ

Source	Sum of Squares	Degrees of freedom	Mean Square	F-value	P-value	
Model	0.2031	20	0.0102	770.24	< 0.0001	significant
T	0.0004	1	0.0004	31.88	< 0.0001	
p	0.0002	1	0.0002	13.77	0.0010	
λ_a	0.1777	1	0.1777	13478.08	< 0.0001	
H_{mem}	0.0045	1	0.0045	340.81	< 0.0001	
ε_{GDL}	0.0111	1	0.0111	840.38	< 0.0001	
$T \cdot p$	0.0000	1	0.0000	1.28	0.2695	
$T \cdot \lambda_a$	6.760E-06	1	6.760E-06	0.5128	0.4805	

$T{\cdot}H_{mem}$	0.0001	1	0.0001	4.67	0.0404
$T{\cdot}\varepsilon_{GDL}$	0.0001	1	0.0001	5.55	0.0267
$p{\cdot}\lambda_a$	1.822E-06	1	1.822E-06	0.1383	0.7131
$p{\cdot}H_{mem}$	0.0000	1	0.0000	1.78	0.1936
$p{\cdot}\varepsilon_{GDL}$	0.0000	1	0.0000	1.31	0.2638
$\lambda_a{\cdot}H_{mem}$	1.000E-08	1	1.000E-08	0.0008	0.9782
$\lambda_a{\cdot}\varepsilon_{GDL}$	1.822E-06	1	1.822E-06	0.1383	0.7131
$H_{mem}{\cdot}\varepsilon_{GDL}$	0.0002	1	0.0002	15.41	0.0006
T^2	8.910E-06	1	8.910E-06	0.6759	0.4188
p^2	2.991E-06	1	2.991E-06	0.2269	0.6380
λ_a^2	0.0057	1	0.0057	434.68	< 0.0001
H_{mem}^2	0.0000	1	0.0000	1.03	0.3196
ε_{GDL}^2	0.0009	1	0.0009	69.48	< 0.0001
Residual	0.0003	25	0.0000		
Lack of Fit	0.0003	20	0.0000		
Pure Error	0.0000	5	0.0000		
Cor Total	0.2034	45			

Standard deviation=0.0036

Predicted residual error of sum of squares (PRESS)=108.4081

R^2(Adequate) = 99.84 % R^2(Predicted) = 99.71 % R^2(Adjusted) = 99.35 %

4.2. Regression model of responses

The regression response surface model for the objective function G (P, η, ψ) is evaluated by:

$$\begin{aligned} G=&a_0+a_1{\cdot}T+a_2{\cdot}p+a_3{\cdot}\lambda_a+a_4\cdot H_{mem}+a_5\cdot\varepsilon_{GDL}\\ &+a_{1,2}T{\cdot}p+a_{1,3}{\cdot}T{\cdot}\lambda_a+a_{1,4}\cdot T\cdot H_{mem}+a_{1,5}\cdot T\cdot\varepsilon_{GDL}\\ &+a_{2,3}{\cdot}p{\cdot}\lambda_a+a_{2,4}\cdot p\cdot H_{mem}+a_{2,5}\cdot p\cdot\varepsilon_{GDL}\\ &+a_{3,4}{\cdot}\lambda_a\cdot H_{mem}+a_{3,5}\cdot\lambda_a\cdot\varepsilon_{GDL}+a_{4,5}\cdot H_{mem}\cdot\varepsilon_{GDL}\\ &+a_{1,1}{\cdot}T^2+a_{2,2}{\cdot}p^2+a_{3,3}{\cdot}\lambda_a{}^2+a_{4,4}\cdot H_{mem}{}^2+a_{5,5}\cdot\varepsilon_{GDL}{}^2 \end{aligned} \tag{30}$$

The regression response surface model coefficients are presented in Table 8. Figure 6 illustrates the relationship between the actual and predicted values of P, η and ψ in the quadratic response surface regression model and their regression curves. The results demonstrate that the predicted values are in good agreement with the actual values, indicating that the established regression response surface model is reliable.

Table 8 Regression coefficient

	Response

Regression coefficient	P (W·cm^{-2})	η	ψ
a_0	+0.5871	+0.2195	+0.3229
a_1	+0.0191	-0.0305	+0.0051
a_2	-0.0052	+0.0000	-0.0034
a_3	+0.0168	-0.0829	-0.1054
a_4	-0.0304	+0.0000	-0.0168
a_5	+0.0479	+0.0000	+0.0263
$a_{1,2}$	+0.0036	+0.0000	+0.0020
$a_{1,3}$	+0.0043	+0.0111	+0.0013
$a_{1,4}$	+0.0065	+0.0000	+0.0039
$a_{1,5}$	+0.0085	+0.0000	+0.0043
$a_{2,3}$	-0.0007	+0.0000	+0.0007
$a_{2,4}$	-0.0045	+0.0000	-0.0024
$a_{2,5}$	-0.0037	+0.0000	-0.0021
$a_{3,4}$	-0.0082	+0.0000	-0.0000
$a_{3,5}$	+0.0137	+0.0000	+0.0007
$a_{4,5}$	-0.0130	+0.0000	-0.0071
$a_{1,1}$	-0.0063	+0.0057	-0.0010
$a_{2,2}$	-0.0011	-0.0001	-0.0006
$a_{3,3}$	-0.0168	+0.0276	+0.0256
$a_{4,4}$	+0.0024	-0.0001	+0.0012
$a_{5,5}$	-0.0182	-0.0001	-0.0102

330

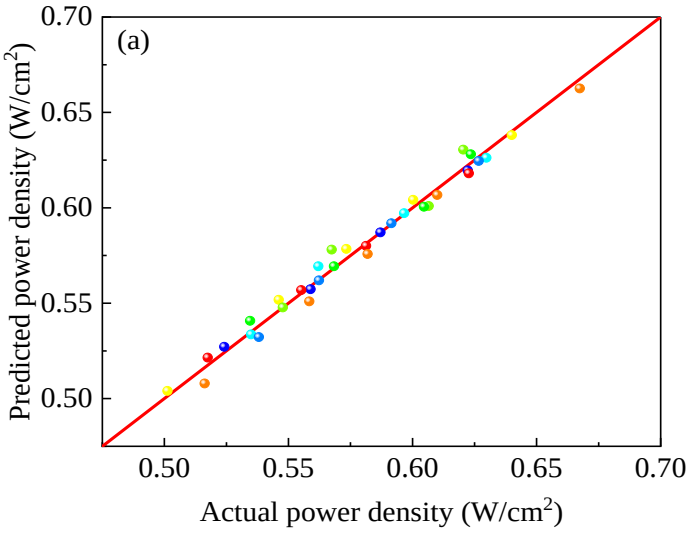

331

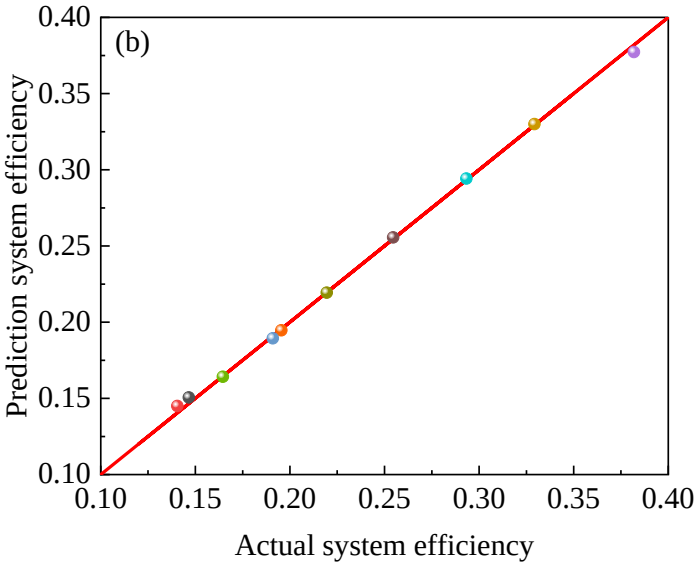

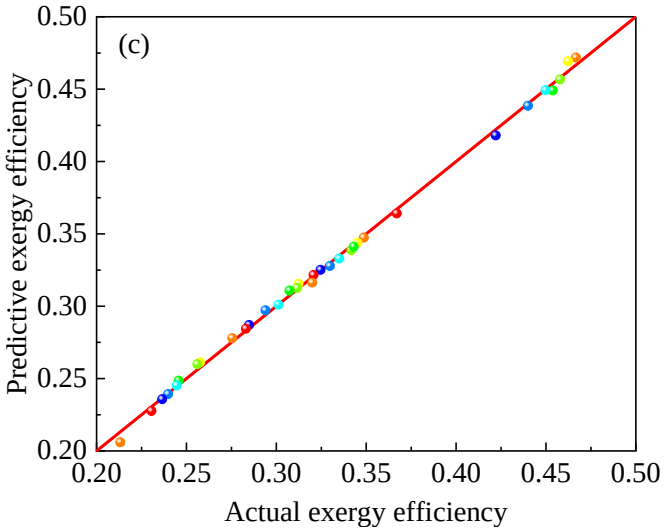

Figure 6 Comparison of actual values versus predicted values in the quadratic response surface regression model and their regression line: (a) P; (b) η;(c) ψ.

4.3. Response surface analysis

Figure 7 shows the effect of the interaction term on the power density P. As shown in Figure 7(j), the interaction between membrane thickness and GDL porosity has the greatest influence on power density. The power density reaches the highest when the film thickness is the lowest and the GDL porosity is the highest. Meanwhile, Figures 7(a) and (c) show that the interaction term of inlet pressure and inlet temperature and the interaction term of inlet pressure and membrane thickness have little influence on power density. Power density decreases with increasing inlet temperature and thickness of the proton exchange membrane. The effect is particularly significant with the thickness

of the membrane. Generally, inlet pressure, anode stoichiometry ratio, thickness of the membrane and GDL porosity have the most significant effects on *P*, while temperature has relatively less effect on *P*. This is primarily because more gas can enter the gas catalytic layer and the GDL porosity increases when the pressure increases, which can also lead to higher current densities and slightly better cell performance. Excessive temperature tends to cause membrane dehydration on the anode side and uneven temperature distribution within the cell, which decreases the performance of the cell. The thickness of the film influences the variation of the film resistance. The film resistance increases and the ohmic polarization intensifies when the thickness increases. On the other hand, the increase in thickness makes the anode side drier. Figures 11 (b), (e), (h) and (i) show that the power density tends to increase and then decrease with the anode stoichiometry ratio. It is mainly related to the hydrogen supply and distribution.

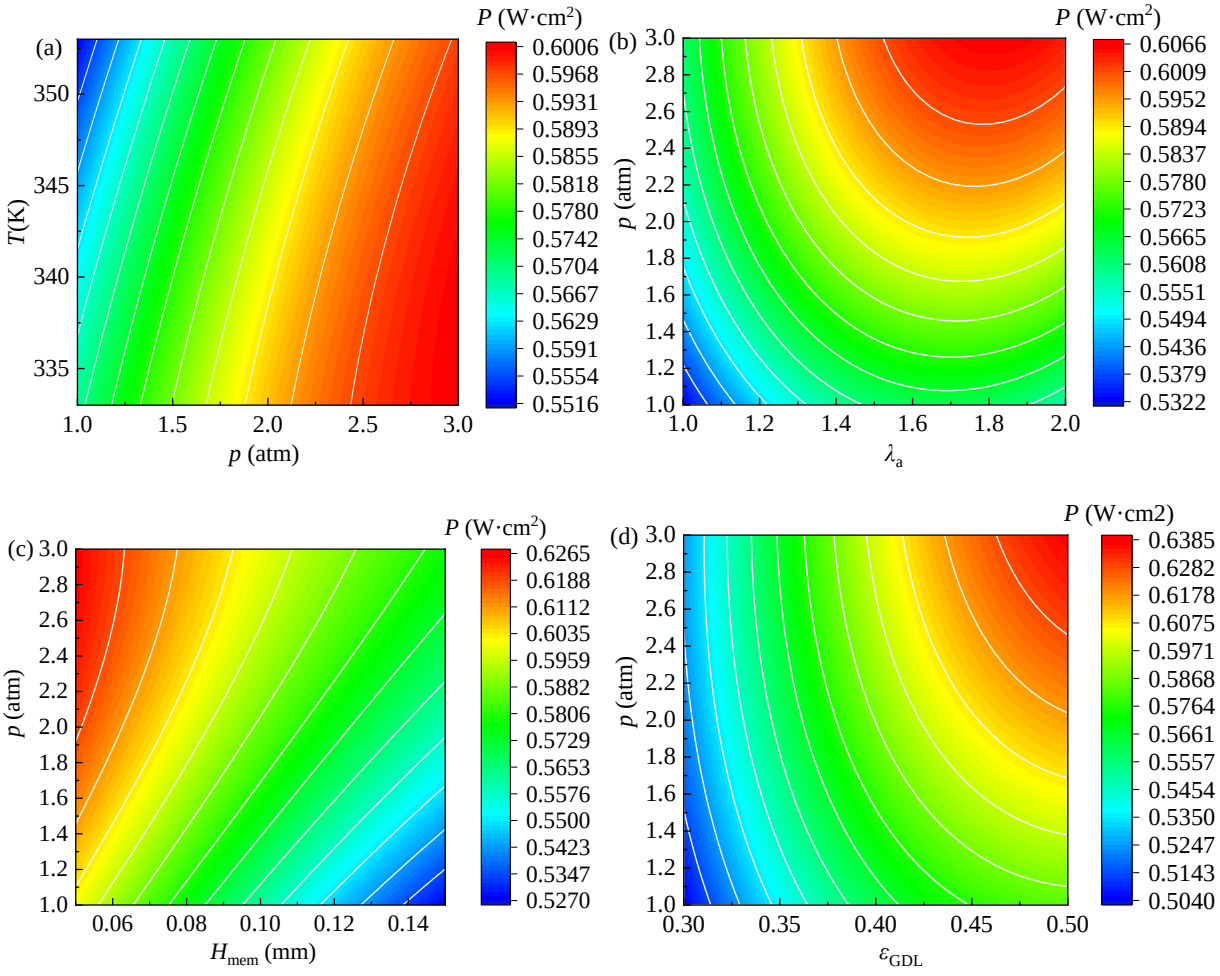

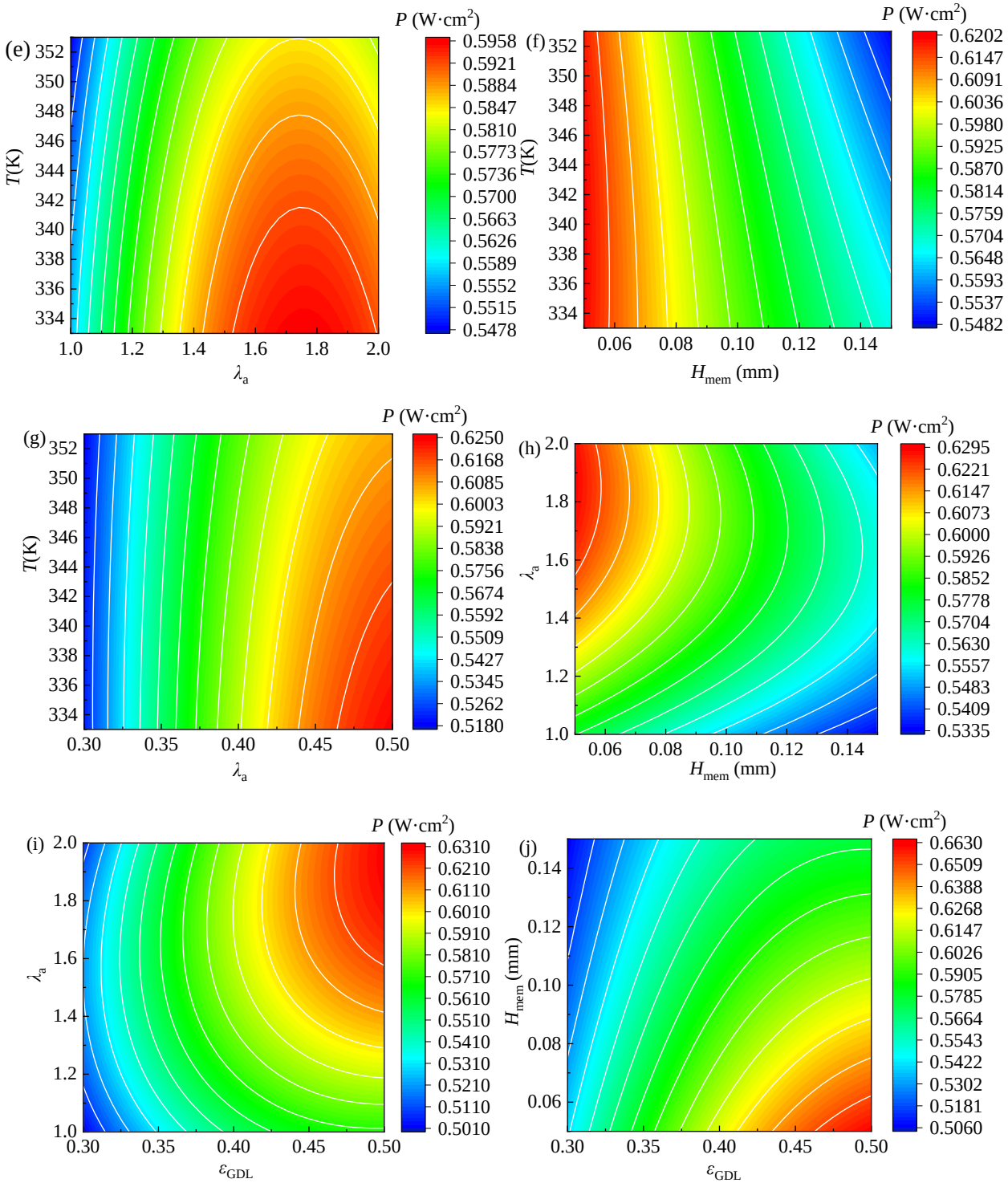

Figure 7 RSM analysis on effect of various parameters on power density: (a) operating temperature and pressure (λ_a=1.5, H_{mem}=0.1 mm, ε_{GDL}=0.4), (b) operating pressure and anode stoichiometry ratio (T=343 K, H_{mem}=0.1 mm, ε_{GDL}=0.4), (c) operating pressure and membrane thickness (T=343 K, λ_a=1.5, ε_{GDL}=0.4), (d) operating pressure and GDL porosity (T=343 K, λ_a=1.5, H_{mem}=0.1 mm), (e) operating temperature and anode stoichiometry ratio (p=2 atm, H_{mem}=0.1 mm,

365 ε_{GDL}=0.4), (f) operating temperature and membrane thickness (p=2 atm, λ_a=1.5, ε_{GDL}=0.4), (g)
366 operating temperature and GDL porosity (p=2 atm, λ_a=1.5, H_{mem}=0.1 mm), (h) anode stoichiometry
367 ratio and membrane thickness (T=343 K, p=2 atm, H_{mem}=0.1 mm), (i) anode stoichiometry ratio and
368 GDL porosity (p=2 atm, T=343 K, H_{mem}=0.1 mm), and (j) membrane thickness and GDL porosity
369 (p=2 atm, T=343 K, λ_a=1.5).

370 Figure 8 illustrates the effect of the interaction term on the system efficiency. As shown in Figure
371 8(b), the interaction between the inlet pressure and anode stoichiometric ratio has the greatest
372 influence on the system efficiency. A smaller inlet pressure reduces the anode stoichiometric ratio and
373 increases the system efficiency. Figures 8(f), (g) and (j) show that the interaction terms of inlet
374 temperature and membrane thickness, inlet temperature and anode stoichiometric ratio, and
375 membrane thickness and GDL porosity have little influence on system efficiency. Meanwhile, the
376 temperature, thickness of the membrane and porosity of the GDL have insignificant effects on the
377 system efficiency (Figures 8 (f), (g) and (j)). The results in Figure 8 clearly indicate that the operating
378 pressure and anode stoichiometry ratio have significant impacts on the system efficiency which
379 decreases as the pressure and anode stoichiometry ratio increase. This is mainly because the power
380 consumption of the compressor increases and the system efficiency becomes lower when the
381 operating pressure increases. The variation in anode stoichiometry ratio is attributed to the fact that
382 the power consumed by the fuel increases when the supply of hydrogen exceeds the demand for the
383 reaction, which in turn leads to a decrease in system efficiency.

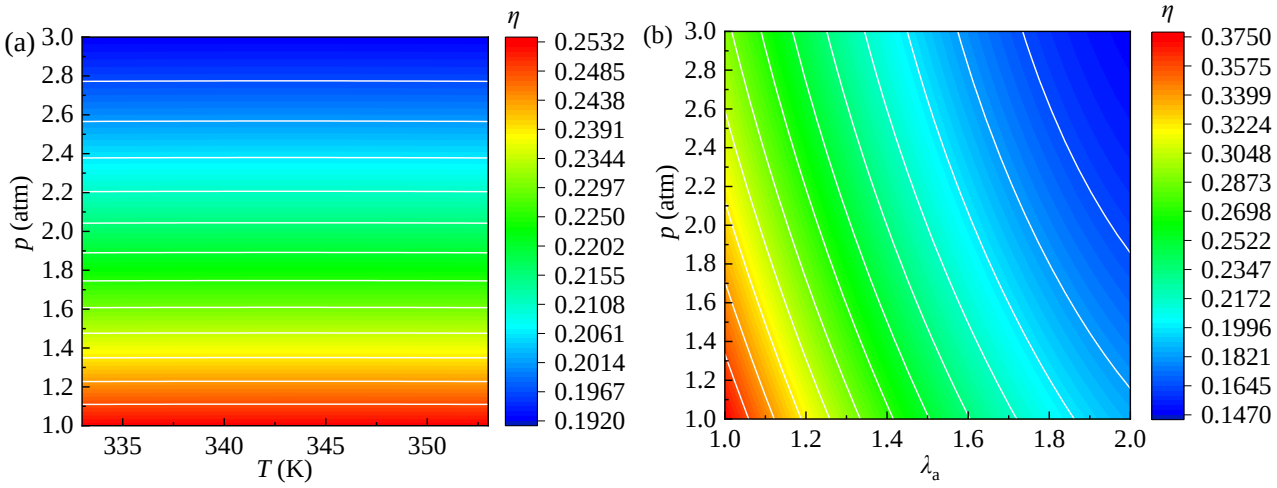
(a)
p (atm)
T (K)
η
(b)
p (atm)
λa
η

384

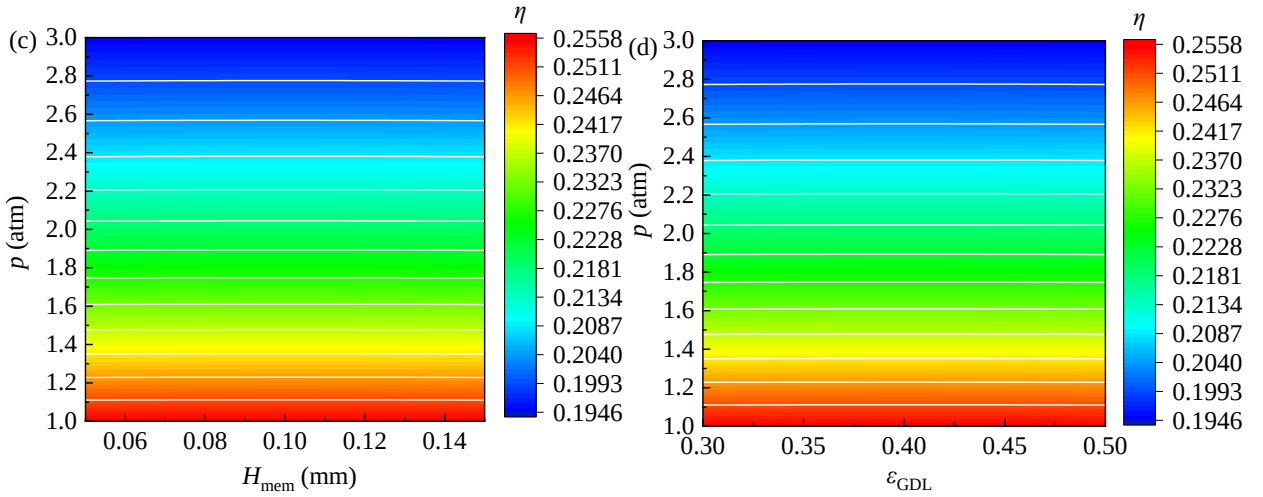
(c)
p (atm)
Hmem (mm)
η
(d)
p (atm)
εGDL
η

385

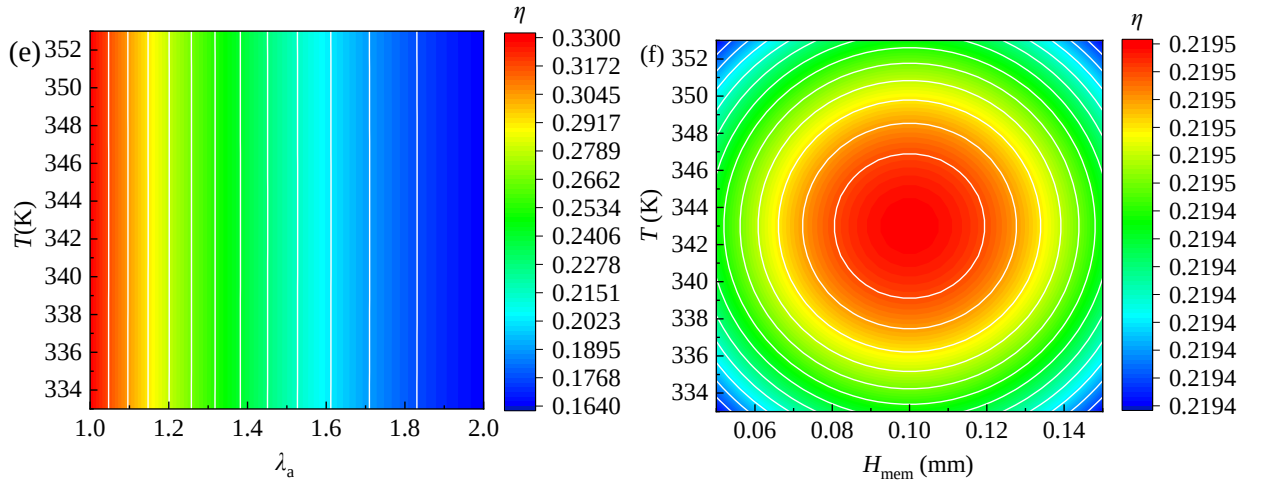
(e)
T(K)
λa
η
(f)
T (K)
Hmem (mm)
η

386

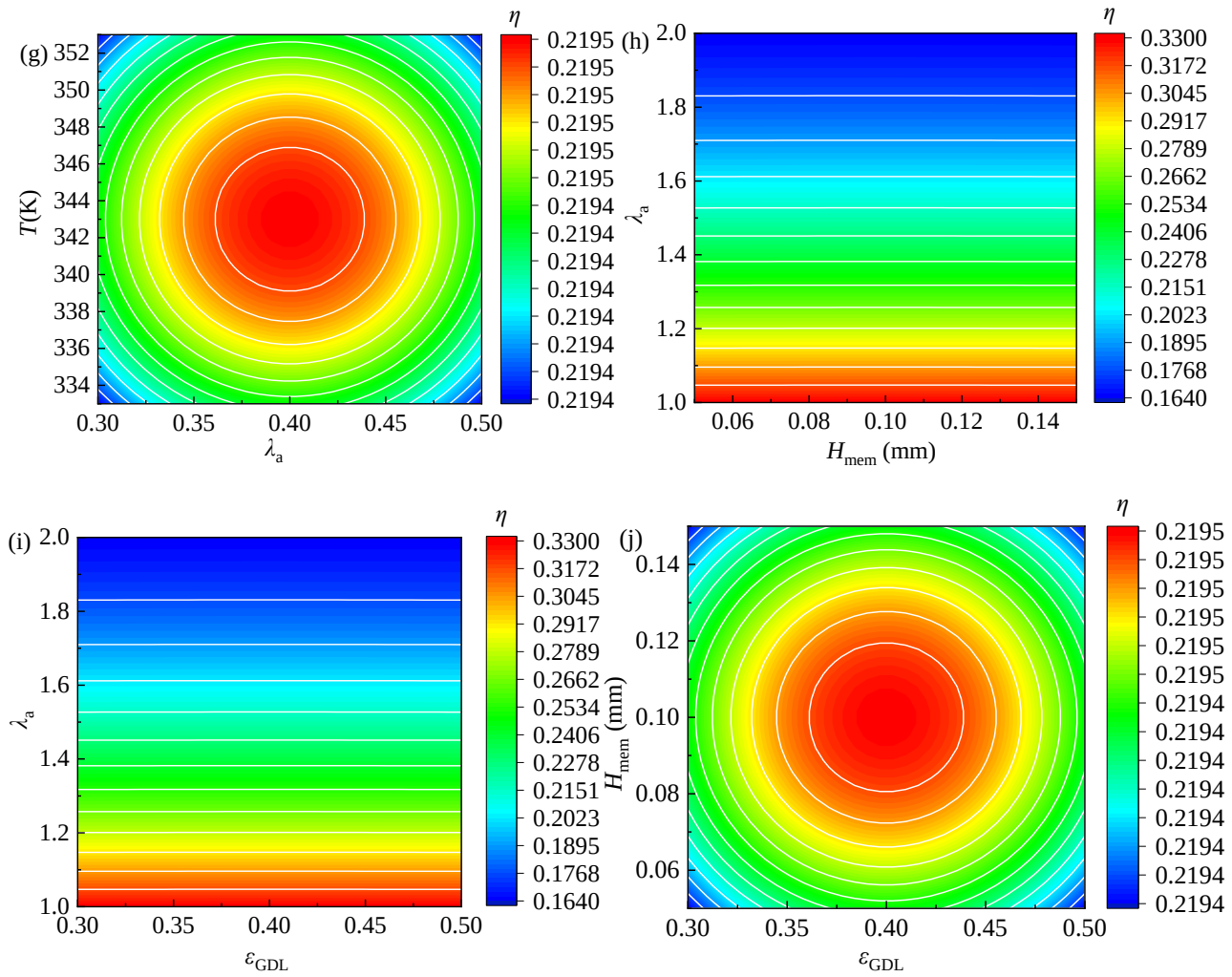

Figure 8 RSM analysis on the effect of various parameters on system efficiency: (a) operating temperature and pressure (λ_a=1.5, H_{mem}=0.1 mm, ε_{GDL}=0.4), (b) operating pressure and anode stoichiometry ratio (T=343 K, H_{mem}=0.1 mm, ε_{GDL}=0.4), (c) operating pressure and membrane thickness (T=343 K, λ_a=1.5, ε_{GDL}=0.4), (d) operating pressure and GDL porosity (T=343 K, λ_a=1.5, H_{mem}=0.1 mm), (e) operating temperature and anode stoichiometry ratio (p=2 atm, H_{mem}=0.1 mm, ε_{GDL}=0.4), (f) operating temperature and membrane thickness (p=2 atm, λ_a=1.5, ε_{GDL}=0.4), (g) operating temperature and GDL porosity (p=2 atm, λ_a=1.5, H_{mem}=0.1 mm), (h) anode stoichiometry ratio and membrane thickness (T=343 K, p=2 atm, H_{mem}=0.1mm), (i) anode stoichiometry ratio and GDL porosity (p=2 atm, T=343 K, H_{mem}=0.1 mm), and (j) membrane thickness and GDL porosity (p=2 atm, T=343 K, λ_a=1.5).

Figure 9 shows the influence of interaction terms on the exergy efficiency. As shown in Figure

9(d), the exergy efficiency gradually increases with the increase of inlet pressure and porosity. This is mainly because a higher inlet pressure or porosity will force more gases to participate in the reaction, leading to higher useful work and exergy efficiency. Figures 9(f), (g) and (h) show that the exergy efficiency decreases with the increase of inlet temperature, film thickness and anode stoichiometry, in particular, effects of the anode stoichiometry are siginficant. It is mainly because higher temperatures and thicker proton exchange membranes reduce the power density and useful work, and thus reducing the exergy efficiency. The interaction between anode stoichiometric ratio and other factors has great influence on the exergy efficiency (Figures 9(b), (e), (h), and (i)). This is mainly because the molar flow rate of hydrogen increases while the hydrogen participating in the reaction remains unchnaged with the increase of anode stoichiometric ratio, leading to the increase of useless work and the decrease of exergy efficiency. As shown in Figure 9(a), the interaction term of inlet pressure and inlet temperature has the lowest impact on exergy efficiency.

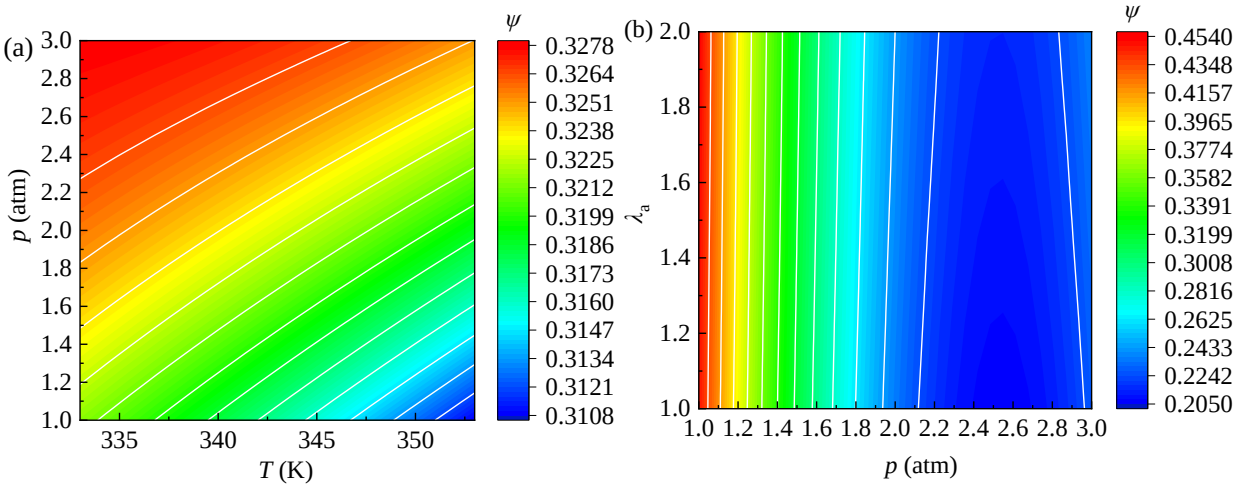

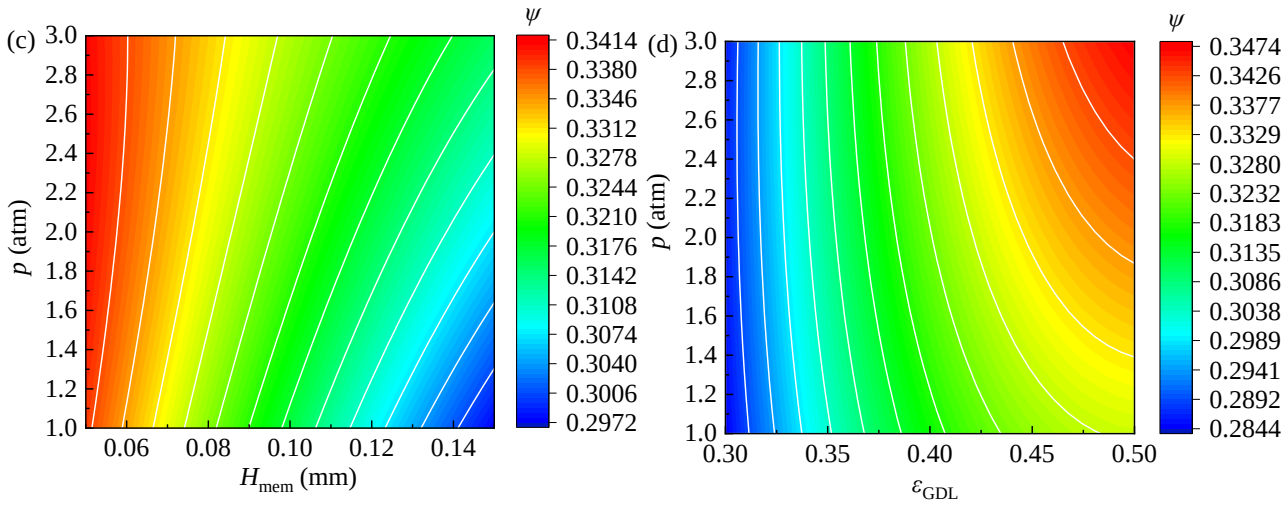
(c)
p (atm)
H_mem (mm)
ψ
(d)
p (atm)
ε_GDL
ψ

413

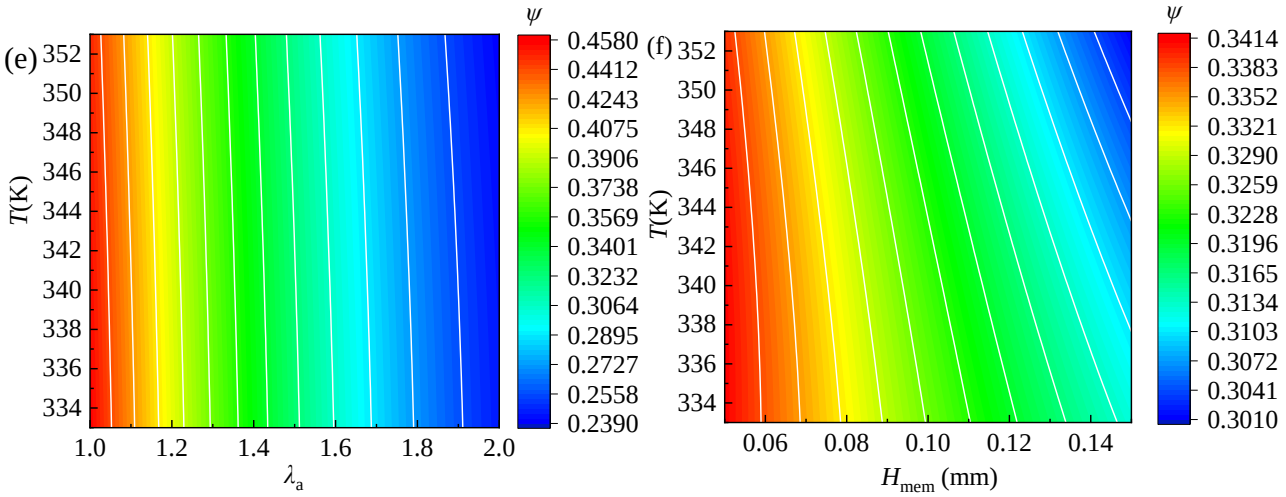
(e)
T(K)
λ_a
ψ
(f)
T(K)
H_mem (mm)
ψ

414

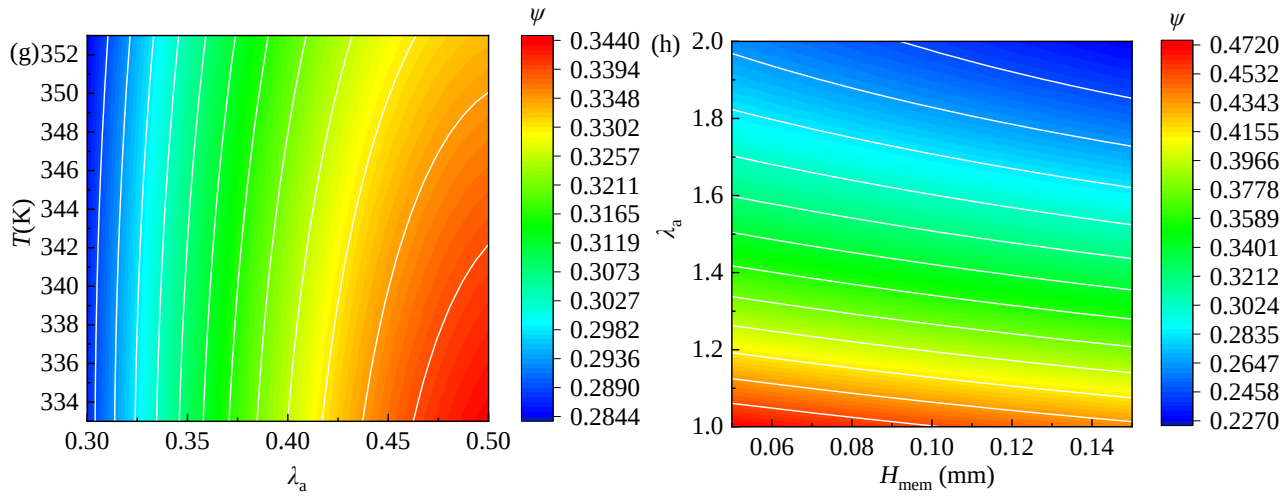
(g)
T(K)
λ_a
ψ
(h)
λ_a
H_mem (mm)
ψ

415

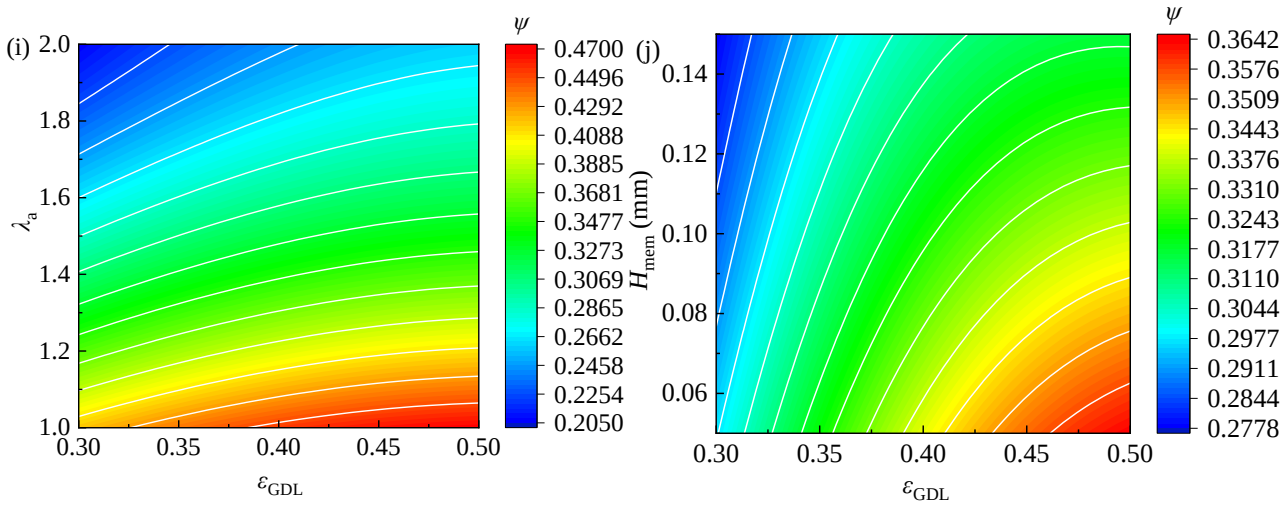

Figure 9 RSM analysis on the effect of various parameters on exergy efficiency: (a) operating temperature and pressure (λ_a=1.5, H_{mem}=0.1 mm, ε_{GDL}=0.4), (b) operating pressure and anode stoichiometry ratio (T=343 K, H_{mem}=0.1 mm, ε_{GDL}=0.4), (c) operating pressure and membrane thickness (T=343 K, λ_a=1.5, ε_{GDL}=0.4), (d) operating pressure and GDL porosity (T=343 K, λ_a=1.5, H_{mem}=0.1 mm), (e) operating temperature and anode stoichiometry ratio (p=2 atm, H_{mem}=0.1 mm, ε_{GDL}=0.4), (f) operating temperature and membrane thickness (p=2 atm, λ_a=1.5, ε_{GDL}=0.4), (g) operating temperature and GDL porosity (p=2 atm, λ_a=1.5, H_{mem}=0.1 mm), (h) anode stoichiometry ratio and membrane thickness (T=343 K, p=2 atm, H_{mem}=0.1mm), (i) anode stoichiometry ratio and GDL porosity (p=2 atm, T=343 K, H_{mem}=0.1 mm), and (j) membrane thickness and GDL porosity (p=2 atm, T=343 K, λ_a=1.5).

4.4. Optimization of designing parameters

The regression model constructed by RSM is shown in Table 8. The NSGA-II method (Table 9) is adopted to solving the three-objective optimization question. The Pareto optimal solution is obtained after the multi-objective optimization of the system (Figure 9). The Pareto surface shows the weighting trade-off between power density, system efficiency and exergy efficiency. It should be noted that the Pareto surface has all the points as optimal values with different weights for these three objectives. At point A, the power density, system efficiency and exergy efficiency are 0.6076 W·cm^{-}

^{2}, 30.99 % and 49.12 %, respectively. Although the exergy efficiency can reach the maximum, the power density and system efficiency are relatively low. For point B, the power density, system efficiency and exergy efficiency are 0.5845 W·cm^{-2}, 36.31 % and 47.96 %, respectively, and the system efficiency can reach the maximum. The power density gradually decreases while increasing the system efficiency [55-57]. For point C, the power density, system efficiency and exergy efficiency are 0.6797 W·cm^{-2}, 17.6% and 33.4%, respectively. Although the power density achieves the highest level, the system efficiency is remarkably low and the exergy efficiency is also not optimal. Point D is closest to the ideal point and thus is selected as the final optimal point. The inclination rate of the evaluation metric and Pareto is milder at point D. Minor changes near point D do not cause the evaluation metric to change drastically. The final optimal power density, system efficiency and exergy efficiency are 0.6327 W·cm^{-2}, 26.16 % and 43.94 %, respectively.

Figure 10 shows the distribution of different PEMFC parameters during the optimization process. The optimal distribution of the operating pressure (Figure 10(a)) is uniformly distributed in the middle range of 1.2-2.5 atm. The majority of the optimal operating temperature values (Figure 10(b)) are around 339 K. Regarding the distribution of the optimal anode stoichiometry ratio (Figure 10(c)), it is found that the range of all the optimal values is uniformly distributed between 1.0 and 1.7. The optimal thickness of the proton exchange membrane is mostly around 0.06 mm (Figure 10(d)) and the optimal GDL porosity is mostly around 0.49 (Figure 10(e)). This indicates that a smaller thickness and a larger porosity improve the overall performance of the system.

Table 10 compares the optimization results, including the operational parameters and performance of the system at points A-D and the base point on the Pareto surface. Point A is the optimal value for the exergy efficiency during optimization. The power density, system efficiency and exergy efficiency are improved by 0.0486 W·cm^{-2}, 11.89 % and 25.47 %, respectively, compared

with the base point. Point B is the optimal value of system efficiency. The power density, system efficiency and exergy efficiency at point B are improved by 0.0255 $W \cdot cm^{-2}$, 17.21 % and 24.31 %, respectively, compared with the base point. Point C is the optimal value of power density. The power density, system efficiency and exergy efficiency at point B are improved by 0.1207 $W \cdot cm^{-2}$ and 9.75 %, respectively, compared with the base point. The system efficiency is 1.5% lower than the base point. Point D is the final optimal point, which provides better performance in all indexes. The power density, system efficiency and exergy efficiency at point D are improved by 0.0737 $W \cdot cm^{-2}$, 7.06 % and 20.29 %, respectively, compared with the base point. The results indicate that the optimization by NSGA-II algorithm has improved the system power density and efficiency at the final optimal point by different degrees.

Table 9 Parameters in NSGA-II

Parameters	Values
Maximum number of iterations	100
Population size	150
Crossover percentage	0.8
Mutation percentage	0.2
Mutation rate	0.2

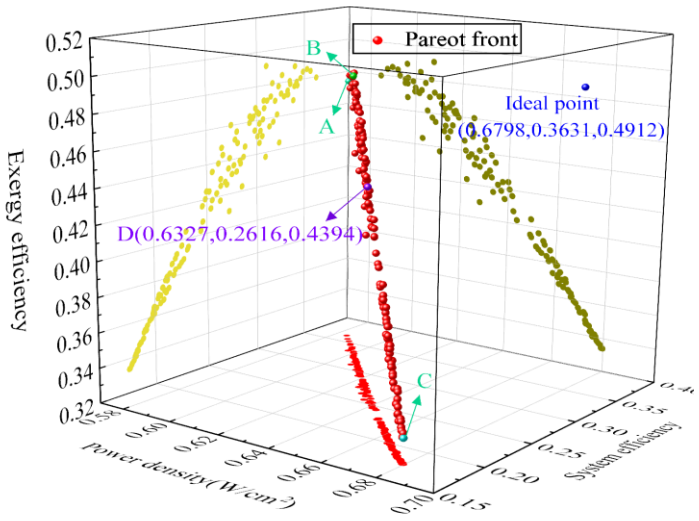

Figure 9 The distribution of Pareto-optimal solutions

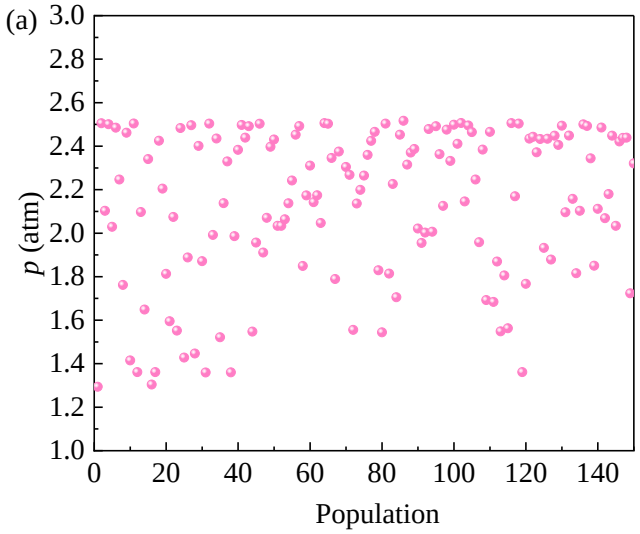

471

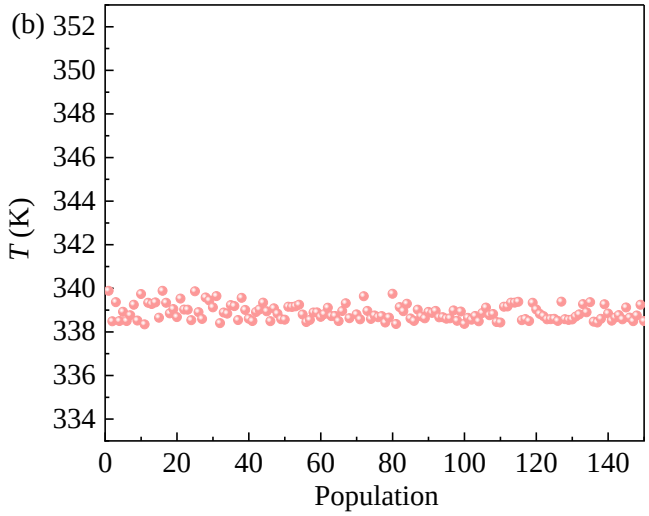

472

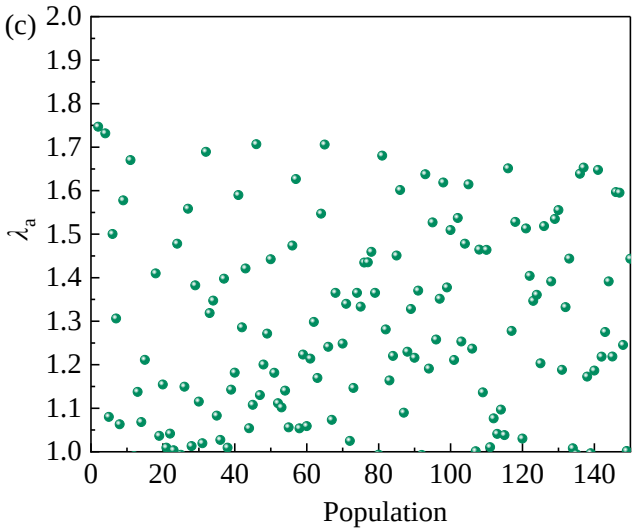

473

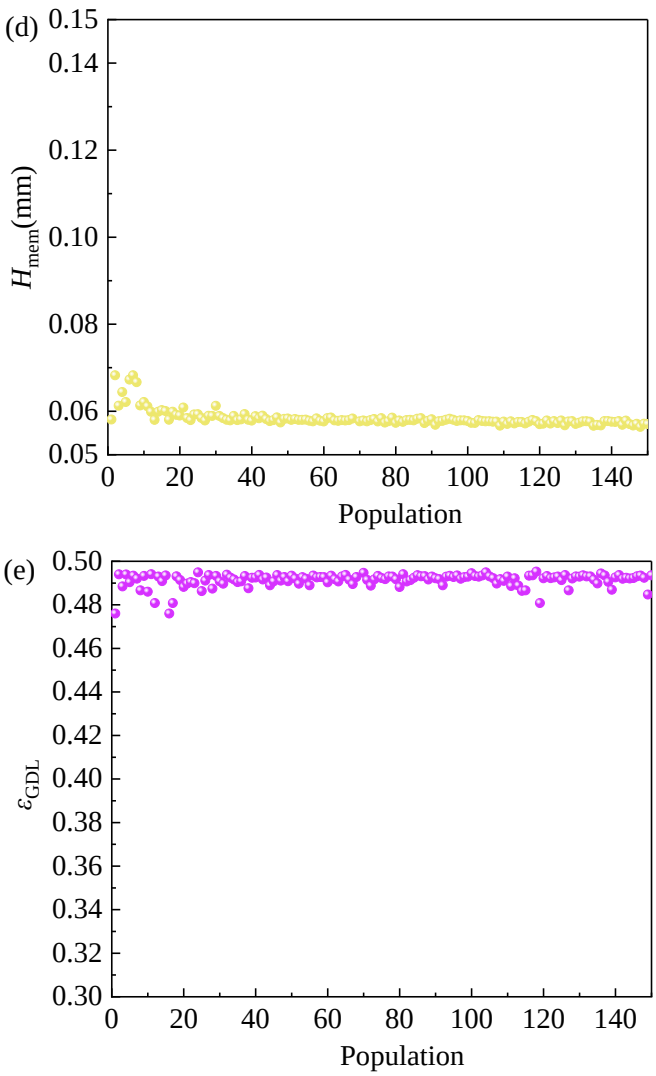

Figure 10 Population distributions of PEMFC operating parameters: (a) operating pressure (p), (b) operating temperature (T), (c) Anode stoichiometric ratio (λ_a), (d) membrane thickness (H_{mem}), and (e) GDL porosity (ε_{GDL}).

Table 10 Comparison of the optimization results

Parameters	Base Case	A	B	C	D
p (atm)	1	2.5021	1.1641	2.9200	2.6498
T (K)	343	340.4938	339.1243	342.8035	341.6210
λ_a	2	1.0020	1.0188	1.6577	1.1808
H_{mem}(mm)	0.1	0.0580	0.0589	0.0570	0.0577
ε_{GDL}	0.4	0.4907	0.4822	0.4931	0.4908
P (W·cm^{-2})	0.5590	0.6076	0.5845	0.6797	0.6327
η	0.1910	0.3099	0.3631	0.1760	0.2616
ψ	0.2365	0.4912	0.4796	0.3340	0.4394

5. Conclusions

In this work, the analysis of variance is used to validate the constructed regression model. The R^2 values of power density, system efficiency and exergy efficiency are 98.63 %, 99.96 %, and 99.84%, respectively, indicating that the quadratic model responds well to the aggregate variation. The F-values of the regression model are 89.82 , 3042.48 and 770.24 for power density, system efficiency and exergy efficiency, respectively. The P-values are less than 0.0001. These results impliy that the regression model has high significance. The significant terms of p with decreasing sensitivity levels are the linear term of p, the linear term of λ_a, the linear term of H_{mem}, the linear term of ε_{GDL}, the squared term of H_{mem} and the squared term of ε_{GDL}. The significant terms of η with decreasing sensitivity levels are the linear term of p, the linear term of λ_a, the interaction term of p and λ_a, the squared term of p, and the squared term of λ_a. The significant terms of ψ with decreasing sensitivity are the linear terms of λ_a, ε_{GDL}, λ_a squared, H_{mem} squared, ε_{GDL} squared and p squared at a time. It is found that p increases with decreasing inlet temperature and thickness of the proton exchange membrane and increasing inlet pressure and porosity of the GDL. While η increases with the decrease of inlet pressure and anode stoichiometry ratio. Exergy efficiency gradually increases with the increase of inlet pressure and porosity, and decreases with the increase of inlet temperature, membrane thickness and anode stoichiometric ratio, in particular, effects of the anode stoichiometric ratio are significant. Finally, multi-objective optimization is performed by NSGA-II to obtain the maximum P, η and ψ. The Pareto solution shows that the optimal power density, system efficiency and exergy efficiency are 0.6327 $W \cdot cm^{-2}$, 26.16 % and 43.94%, respectively, which are 13.18 %, 7.06 % and 20.29 % better than the initial direct current channel. The corresponding design variables are p=2.6498 atm, T=341.621 K, λ_a =1.1808, H_{mem} =0.0577 mm and ε_{GDL} =0.4908. Although this work greatly improves the multi-objective of the PEMFC performance, future works are needed for further improvement of PEMFC. In particular, collaborative optimization on cathode gas channel, anode gas

channel, gas catalytic layer, GDL and proton exchange membrane can be realized for higher power density, system efficiency and exergy efficiency.

Conflict of Interests

The authors declare that they have no known competing financial interests or personal relationships that could have appeared to influence the work reported in this work.

Acknowledgements

Dr. Wei Zuo gratefully acknowledges the financial support provided by Wuhan University of Science and Technology (No. 1010010) and Wuhan Yellow Crane Talents Program. Dr. Yuhan Huang is a recipient of the ARC Discovery Early Career Research Award (DE220100552)

References

[1] George S, Sehgal N, Rana KPS, Kumar V. A Comprehensive Review on Modelling and Maximum Power Point Tracking of PEMFC. Cleaner Energy Systems 2022;3:100031.

[2] Wang B, Zhao D, Li W, Wang Z, Huang Y, You Y, Becker S. Current technologies and challenges of applying fuel cell hybrid propulsion systems in unmanned aerial vehicles. Progress in Aerospace Sciences 2020;116:100620.

[3] Jiao K, Xuan J, Du Q, Bao Z, Bao ZM, Xie B,Wang B,Zhao Y, Fan LH, Wang HZ, Hou ZJ, Hou S, Brandon NP, Yin Y, Guiver MD. Designing the next generation of proton-exchange membrane fuel cells. Nature 2021;595(7867):361-369.

[4] Zhao D, Guan Y, Reinecke A. Characterizing hydrogen-fuelled pulsating combustion on thermodynamic properties of a combustor. Communications Physics 2019;2(1):1-10.

[5] Muduli RC, Kale P. Silicon nanostructures for solid-state hydrogen storage: A review. International Journal of Hydrogen Energy 2023;48(4):1401-1439.

[6] Cai T, Zhao D. Effects of fuel composition and wall thermal conductivity on thermal and NOx emission performances of an ammonia/hydrogen-oxygen micro-power system. Fuel Processing Technology 2020;209:106527.

[7] Ji C, Zhao D, Li X, Li S, Li J. Nonorthogonality analysis of a thermoacoustic system with a premixed V-shaped flame. Energy conversion and management 2014;85:102-111.

[8] Chen KI, Winnick J, Manousiouthakis VI. Global optimization of a simple mathematical model for a proton exchange membrane fuel cell. Computers & chemical engineering 2006;30(8):1226-1234.

[9] Sohani A, Naderi S, Torabi F. Comprehensive comparative evaluation of different possible optimization scenarios for a polymer electrolyte membrane fuel cell. Energy Conversion and Management 2019;191:247-260.

[10] Chen X, Long S, He L, Wang CX, Chai F, Kong XZ, Wan ZM, Song XX, Tu ZK. Performance evaluation on thermodynamics-economy-environment of PEMFC vehicle power system under dynamic condition. Energy Conversion and Management 2022;269:116082.

[11] Chandrasekaran R, Bi W, Fuller TF. Robust design of battery/fuel cell hybrid systems—Methodology for surrogate models of Pt stability and mitigation through system controls. Journal of Power Sources 2008;182(2):546-557.

[12] Mohammedi A, Sahli Y, Moussa HB. 3D investigation of the channel cross-section configuration effect on the power delivered by PEMFCs with straight channels. Fuel 2020;263:116713.

[13] Chu T, Xie M, Yu Y, Wang DJ, Li B, Ming PW, Zhang CM. Experimental study of the influence of dynamic load cycle and operating parameters on the durability of PEMFC. Energy

2022;239:122356.

[14] Dhanya AR, Ganguly D, Sundara R. High temperature annealed (002) oriented WO3 nanoplatelets with uniform Pt decoration as durable carbon free anode electrocatalyst for PEMFC application. International Journal of Hydrogen Energy 2022;47(59):24978-24990.

[15] Chen H, Guo H, Ye F, Ma CF. Experimental investigations on cell performance of proton exchange membrane fuel cells with orientated-type flow channels. Journal of Energy Engineering 2020;146(6):04020062.

[16] Chen H, Guo H, Ye F, Ma CF. An experimental study of cell performance and pressure drop of proton exchange membrane fuel cells with baffled flow channels. Journal of Power Sources 2020;472:228456.

[17] Kuo J K. The effects of buoyancy on the performance of a PEM fuel cell with a wave-like gas flow channel design by numerical investigation. International Journal of Heat and Mass Transfer 2007;50(21-22):4166-4179.

[18] Liao Z, Wei L, Dafalla AM, Guo J, Jiang F. Analysis of the impact of flow field arrangement on the performance of PEMFC with zigzag-shaped channels. International Journal of Heat and Mass Transfer 2021;181:121900.

[19] Xu Y, Chang G, Fan R, Cai T. Effects of various operating conditions and optimal ionomer-gradient distribution on temperature-driven water transport in cathode catalyst layer of PEMFC. Chemical Engineering Journal 2023;451:138924.

[20] Hu D, Wang Y, Li J, Yang Q, Wang J. Investigation of optimal operating temperature for the PEMFC and its tracking control for energy saving in vehicle applications. Energy Conversion and Management 2021;249:114842.

[21] Ouaidat G, Cherouat A, Kouta R, Chamoret D. Study of the effect of mechanical uncertainties

parameters on performance of PEMFC by coupling a 3D numerical multiphysics model and design of experiment. International Journal of Hydrogen Energy 2022;47(56):23772-23786.

[22] Seyhan M, Akansu YE, Murat M, Korkmaz Y, Akansu SO. Performance prediction of PEM fuel cell with wavy serpentine flow channel by using artificial neural network. International journal of hydrogen energy 2017;42(40):25619-25629.

[23] Saleh IM, Ali R, Zhang H. Environmental Impact of High Altitudes on the Operation of PEM Fuel Cell Based UAS. Energy and Power Engineering 2018;10(03):87-105.

[24] Ubong EU, Shi Z, Wang X. Three-dimensional modeling and experimental study of a high temperature PBI-based PEM fuel cell. Journal of The Electrochemical Society 2009;156(10):B1276.

[25] Haraldsson K, Alvfors P. Effects of ambient conditions on fuel cell vehicle performance. Journal of power sources 2005; 145(2): 298-306.

[26] Ghasabehi M, Jabbary A, Shams M. Cathode side transport phenomena investigation and Multi-Objective optimization of a tapered parallel flow field PEMFC. Energy Conversion and Management 2022;265:115761.

[27] Li H, Xu B, Lu G, Du CH, Huang N. Multi-objective optimization of PEM fuel cell by coupled significant variables recognition, surrogate models and a multi-objective genetic algorithm. Energy Conversion and Management 2021;236:114063.

[28] Son J, Um S, Kim YB. Numerical analysis of the effect of anisotropic gas diffusion layer permeability on polymer electrolyte membrane fuel cell performance with various channel types. Fuel 2021;289:119888.

[29] Cho J, Kim H S, Min K. Transient response of a unit proton-exchange membrane fuel cell under various operating conditions. Journal of Power Sources 2008;185(1):118-128.

596 [30] Sim J, Kang M, Kim J, Min K. Effects of operating conditions, various properties of the gas
597 diffusion layer, and shape of endplate on the open-cathode proton exchange membrane fuel cell
598 performance. Renewable Energy 2022;196:40-51.
599 [31] Wang Y, Zhang H, Qi J, Han K, He S, Guo C, Cheng S, Gao M. Thermodynamic and exergy
600 analysis of a novel PEMFC-ORC-MH combined integrated energy system. Energy Conversion
601 and Management 2022;264:115709.
602 [32] Liu G, Qin Y, Li M, Liu Y, Zheng J, Liu X, Yin Y. Performance analysis and optimization of a
603 PEMFC-CAORC system based on 3D construction method of thermodynamic cycle. Energy
604 Conversion and Management 2021;247:114730.
605 [33] Wang Z, Mao J, He Z, Liang F. Energy-exergy analysis of an integrated small-scale LT-PEMFC
606 based on steam methane reforming process. Energy Conversion and Management 2021; 246:
607 114685.
608 [34] Authayanun S, Hacker V. Energy and exergy analyses of a stand-alone HT-PEMFC based
609 trigeneration system for residential applications. Energy Conversion and Management
610 2018;160:230-242.
611 [35] Chen X, Long S, He L, Wang CX, Chai F, Kong XZ, Wan ZM, Song XX, Tu ZK. Performance
612 evaluation on thermodynamics-economy-environment of PEMFC vehicle power system under
613 dynamic condition. Energy Conversion and Management 2022;269:116082.
614 [36] Ay M, Midilli A, Dincer I. Exergetic performance analysis of a PEM fuel cell. International
615 journal of energy research 2006;30(5):307-321.
616 [37] Kazim A. Exergy analysis of a PEM fuel cell at variable operating conditions. Energy conversion
617 and management 2004;45(11-12):1949-1961.
618 [38] Luo L, Wang H, Li C, Hu Y. Life cycle assessment of methanol vehicles from energy,

environmental and economic perspectives. Energy Reports 2022;8:5487-5500.

[39] Zhao J, Cai S, Huang X, Luo X, Tu Z. 4E analysis and multiobjective optimization of a PEMFC-based CCHP system with dehumidification. Energy Conversion and Management 2021;248:114789.

[40] Kanani H, Shams M, Hasheminasab M, Bozorgnezhad A. Model development and optimization of operating conditions to maximize PEMFC performance by response surface methodology. Energy Conversion and Management 2015;93:9-22.

[41] Li H, Xu B, Lu G, Du CH, Huang N. Multi-objective optimization of PEM fuel cell by coupled significant variables recognition, surrogate models and a multi-objective genetic algorithm. Energy Conversion and Management 2021;236:114063.

[42] Silva V, Eusébio D, Cardoso J, Zhiani M, Majidi S. Targeting optimized and robust operating conditions in a hydrogen-fed Proton Exchange Membrane Fuel Cell. Energy Conversion and Management 2017;154:149-156.

[43] Sohani A, Naderi S, Torabi F. Comprehensive comparative evaluation of different possible optimization scenarios for a polymer electrolyte membrane fuel cell. Energy Conversion and Management 2019;191:247-260.

[44] Yao J, Wu Z, Wang H, Yang FS, Xuan J, Xing L, Ren JW, Zhang ZX. Design and multi-objective optimization of low-temperature proton exchange membrane fuel cells with efficient water recovery and high electrochemical performance. Applied Energy 2022;324:119667.

[45] Chen X, Li W, Gong G, Wan ZM, Tu ZK. Parametric analysis and optimization of PEMFC system for maximum power and efficiency using MOEA/D. Applied Thermal Engineering 2017;121:400-409.

[46] Manso AP, Marzo FF, Barranco J, Garikano X, Mujika MG. Influence of geometric parameters

642 of the flow fields on the performance of a PEM fuel cell. A review. International Journal of
643 Hydrogen Energy 2012;37(20):15256-15287.
644 [47] Pei P, Yang W, Li P. Numerical prediction on an automotive fuel cell driving system.
645 International Journal of Hydrogen Energy 2006;31(3):361-369.
646 [48] Box GEP, Wilson KB. On the experimental attainment of optimum conditions// Breakthroughs
647 in statistics. Springer, New York, NY 1992:270-310.
648 [49] Mei B, Barnoon P, Toghraie D, Su C, Nguyen HC, Khan A. Energy, exergy, environmental and
649 economic analyzes (4E) and multi-objective optimization of a PEM fuel cell equipped with
650 coolant channels. Renewable and Sustainable Energy Reviews 2022;157:112021.
651 [50] Deng B, Huang W, Jian Q. An open-cathode PEMFC efficiency optimization strategy based on
652 exergy analysis and data-driven modeling. Energy 2023;264:126148.
653 [51] Antonacci P, Chevalier S, Lee J, Ge N, Hinebaugh J, Yip R, Tabuchi Y, Kotaka T, Bazylak A.
654 Balancing mass transport resistance and membrane resistance when tailoring microporous layer
655 thickness for polymer electrolyte membrane fuel cells operating at high current densities.
656 Electrochimica Acta 2016;188:888-897.
657 [52] Ang SMC, Brett DJL, Fraga ES. A multi-objective optimisation model for a general polymer
658 electrolyte membrane fuel cell system. Journal of power sources 2010;195(9):2754-2763.
659 [53] Wang Z, Mao J, He Z, Liang F. Energy-exergy analysis of an integrated small-scale LT-PEMFC
660 based on steam methane reforming process. Energy Conversion and Management
661 2021;246:114685.
662 [54] Samsun RC, Pasel J, Janßen H, Lehnert W, Peters R, Stolten D. Design and test of a 5 kWe high-
663 temperature polymer electrolyte fuel cell system operated with diesel and kerosene. Applied
664 energy 2014;114:238-249.

665 [55] Zuo W, Wang Z, E J, Li Q, Cheng Q, Wu Y, Zhou K. Numerical investigations on the
666 performance of a hydrogen-fueled micro planar combustor with tube outlet for
667 thermophotovoltaic applications. Energy 2023;263:125957.
668 [56] Zuo W, Li D, E J, Xia Y, Li Q, Quan Y, Zhang G. Parametric study of cavity on the performance
669 of a hydrogen-fueled micro planar combustor for thermophotovoltaic applications. Energy
670 2023;263:126028.
671 [57] Zuo W, Chen Z, E J, Li Q, Zhang G, Huang Y. Effects of structure parameters of tube outlet on
672 the performance of a hydrogen-fueled micro planar combustor for thermophotovoltaic
673 applications. Energy 2023;266:126434.